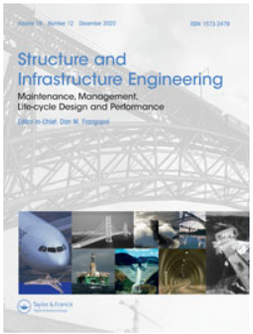

Taylor & Francis
Taylor & Francis Group

Structure and Infrastructure Engineering
Maintenance, Management, Life-Cycle Design and Performance

ISSN: 1573-2479 (Print) 1744-8980 (Online) Journal homepage: https://www.tandfonline.com/loi/nsie20

Development limitations of compressive arch and catenary actions in reinforced concrete special moment resisting frames under column-loss scenarios

Tarek Almusallam, Yousef Al-Salloum, Hussein Elsanadedy, Ngo Tuan, Priyan Mendis & Husain Abbas

To cite this article: Tarek Almusallam, Yousef Al-Salloum, Hussein Elsanadedy, Ngo Tuan, Priyan Mendis & Husain Abbas (2020) Development limitations of compressive arch and catenary actions in reinforced concrete special moment resisting frames under column-loss scenarios, Structure and Infrastructure Engineering, 16:12, 1616-1634, DOI: 10.1080/15732479.2020.1719166

To link to this article: https://doi.org/10.1080/15732479.2020.1719166

STRUCTURE AND INFRASTRUCTURE ENGINEERING
2020, VOL. 16, NO. 12, 1616–1634
https://doi.org/10.1080/15732479.2020.1719166

Development limitations of compressive arch and catenary actions in reinforced concrete special moment resisting frames under column-loss scenarios

Tarek Almusallam[a], Yousef Al-Salloum[a], Hussein Elsanadedy[a], Ngo Tuan[b], Priyan Mendis[b] and Husain Abbas[a]

[a]Chair of Research and Studies in Strengthening and Rehabilitation of Structures, Department of Civil Engineering, College of Engineering, King Saud University, Riyadh, Saudi Arabia; [b]Department of Infrastructure Engineering, The University of Melbourne, Melbourne, Victoria, Australia

ABSTRACT

The progressive collapse of structures, and reinforced concrete (RC) in particular, has recently been the focus of practicing structural engineers. This paper aims to study numerically the limitations for the development of compressive arch and catenary actions in RC special moment resisting frames (SMRFs) when exposed to abrupt column-loss scenarios due to the risk of accidental events such as blast attacks. A finite element (FE) model that incorporates nonlinear materials behavior, bond-slip behavior at the concrete-to-steel rebar interface, and strain rate effect was prepared to study the behavior of RC frame assemblies under column-removal scenarios. The FE model was calibrated against a model-scale RC SMRF specimen tested for a column-removal scenario. The calibrated model was employed for studying the effect of various assembly types, viz. 3D assembly with slabs, 3D assembly without slabs, and 2D assembly on the behavior of RC SMRFs under a column-removal scenario. For the 2D assembly, different parameters were varied for numerical study. A new relative stiffness parameter was first introduced in this study to evaluate the potential for the development of catenary and compressive arch actions in RC SMRFs under abrupt column-removal scenarios.

ARTICLE HISTORY
Received 13 January 2019
Revised 10 November 2019
Accepted 14 December 2019

KEYWORDS
Progressive collapse; special moment resisting frames; compressive arch action; catenary action; column-removal scenario; risk analysis

1. Introduction

Progressive collapse is a chain of local and consequent global failures owing to the local failure of structural members caused by anomalous loads. For inhibiting the progressive collapse, enough redundancy is required for having alternative load path, even if a vertical load-carrying element is lost. For avoiding progressive collapse, different codes (ACI 318-11, 2011; ASCE/SEI 7-16, 2016; CEN, 2002; DOD, 2005; GSA, 2013; IBC, 2000; ISC, 2001; NRCC, 1995) require the setup of connecting members, the selection of appropriate plans, consideration of load combinations covering column-loss scenarios, and methods of introducing alternate load transfer paths. Some concepts for minimizing the potential of progressive collapse in RC structures have also been recently patented (U.S. Patent No. 9765521 B1, 2017 (Abbas et al. 2017); Chinese Patent No. CN 203230191U, 2013).

The progressive collapse behaviour was incorporated in various design codes and guidelines (ACI 318-11, 2011; ASCE/SEI 7-16, 2016; CEN, 2002; DOD, 2005; GSA, 2013; IBC, 2000; ISC, 2001; NRCC, 1995) through a notional column-loss scenario, which were based on early progressive collapse incidents reported in the past (e.g. Almusallam, Elsanadedy, Abbas, Alsayed, & Al-Salloum, 2010a; Pearson & Delatte, 2005). Significant work has been dedicated towards studying the progressive collapse potential in RC moment-resisting frames (e.g. Almusallam, Elsanadedy, Abbas, Alsayed, et al., 2010a; Al-Salloum et al., 2015, Al-Salloum, Abbas, Almusallam, Ngo, & Mendis, 2017, Al-Salloum, Alrubaidi, Elsanadedy, Almusallam, & Iqbal, 2018; Ellingwood, 2006; Elsanadedy, Almusallam, Alharbi, Al-Salloum, & Abbas, 2014, Elsanadedy, Almusallam, Al-Salloum, & Abbas, 2017; Kim & Kim, 2009; Liu, Xu, & Grierson, 2008; Marjanishvili & Agnew, 2006; Pearson & Delatte, 2005; Tsai & Lin, 2008).

The contribution of catenary and compressive arch actions to resist progressive collapse of steel and RC structures has been recently investigated experimentally and numerically by some researchers (e.g. Kang & Tan, 2016; Kim & An, 2009; Milner et al., 2007; Sasani, Bazan, & Sagiroglu, 2007, Sasani & Kropelnicki, 2008; Yi, He, Xiao, & Kunnath, 2008; Yu & Tan, 2014, 2017). Choi and Kim (2011) demonstrated through experiments performed on RC beam-column sub-assemblages, the role of seismic reinforcement detailing in resisting progressive collapse through the development of catenary actions in beams. In another experimental study on RC frames by Yu and Tan (2013), the effect of seismic detailing in resisting the progressive collapse was also highlighted. The Compressive Arch Action (CAA) and the catenary action were found to considerably improve capacity to resist progressive collapse. Kim and Yu (2012) investigated numerically the influence of the amount of reinforcement in resisting progressive collapse of RC moment frames. The flexural reinforcement was shown to

CONTACT Yousef Al-Salloum ysalloum@ksu.edu.sa

increase the catenary action, whereas, the shear reinforcement helped in the formation of the catenary action.

The role of reinforcement detailing in resisting progressive collapse in RC frames was also investigated experimentally by the authors through tests performed at King Saud University (Almusallam, Al-Salloum, Ngo, Mendis, & Abbas, 2017). Two types of rebar detailing were used – one conforming to the ordinary moment-resisting frames (OMRF) and the other conforming to special moment-resisting frames (SMRF) (ACI 318-11,11, 2011). The scaled frames were tested for a column-removal scenario. The experiments gave rise to a better understanding on the effect of connection detailing in the RC floor systems in terms of mitigating the progressive collapse mechanism.

In the research performed at NIST (Bao, Lew, & Kunnath, 2014; Lew, Bao, Pujol, & Sozen, 2014), two full-scale RC beam-column assemblies were tested under a column-removal scenario representing portion of the exterior moment-resisting frames of two prototype 10-story RC frame buildings designed based on intermediate and special moment frames respectively. The frames were tested under monotonically increasing vertical displacement of the middle column. The ultimate loads of the tested specimens were mainly resisted through catenary action developed in beams. The rotations at the ends of catenary beams were much larger (7 to 8 times) than those specified in ASCE/SEI 41-06 (2006).

In addition to the experimental study, two types of numerical models were also developed – one detailed model with fine mesh of solid elements of concrete and beam elements of reinforcement and the second simplified model using beam and spring elements. The first model was used to represent the nonlinear material behavior of reinforced concrete, whereas the second model was assumed to represent the nonlinear behavior of structural components. The numerical results were validated using the test results of their study.

Lim, Tan, and Lee (2017) tested four RC frame specimens with two each under corner and exterior column loss scenarios. Two types of frames were used - skeletal frame and frame-slab assembly. The test results were helpful in studying the columns and beams interaction. The comparison between the two types of frames was used to assess the contribution of slab in progressive collapse mechanism. Lu et al. (2017) tested five 1/3 scaled RC framed specimens, including one skeletal beam specimen without slab and four beam-slab specimens under exterior column loss scenario. They investigated the effect of beam depth, slab thickness and reinforcement detailing on the progressive collapse resistance of frames. The presence of RC slabs increased the collapse resistance by 146% for small deformations and 98% under the catenary action as compared to the skeletal beam frame. The numerical modeling of these test results was reported in (Yu, Luo, & Li, 2018). The numerical models were used to conduct parametric study for assessing the effect of loading schemes, lateral restraint provided by the substructure boundaries, reinforcement detailing of slabs, and slab thickness.

The objective of this paper is to study numerically the limitations for the development of compressive arch and catenary actions in RC special moment resisting frames (SMRFs) when exposed to column-loss scenarios. A finite element (FE) model was established using LS-DYNA software (2007) to predict the behaviour of RC frame assemblies under a column-loss scenario. The model incorporates the nonlinear materials behaviour, bond-slip behaviour at the concrete-to-steel rebar interface, and strain rate effect. The results of the model were calibrated with the test results of the SMRF specimen tested previously by the authors (Almusallam et al., 2017).

The calibrated model was then used to study the effect of various assembly types, viz. 3D assembly with slabs, 3D assembly without slabs and 2D assembly on the behaviour of RC SMRFs under a middle column-loss scenario. For the 2D assembly, different parameters were numerically studied, viz. the stress development in the rebars at exterior joints, axial load acting on the outer columns, and stiffness of the joint next to the removed column. A new relative stiffness parameter was used to assess the development potential of catenary and compressive arch actions in RC SMRFs under abrupt column-removal scenarios.

2. Experimental program

To achieve the objective of this study, experimental data is required for validating the FE model. A single story scaled model of a RC SMRF building, tested at King Saud University by the authors (Almusallam et al., 2017) under a column-removal scenario, has been employed. The test specimen (denoted as SMRF) was designed at a quarter-scale of the prototyped exterior bays (two-bay by one-bay). The selected prototype assembly was selected as an eight-story SMRF building located at the west coast of Saudi Arabia. As per the Saudi Building Code SBC 301 (2007) requirements, the parameters for the earthquake resistant design of the building are: Occupancy Category III, Site Class E and Seismic Design Category C. All spans of the prototype building were 8.0 m.

The RC framed building was designed as per the ACI 318-11 code (2011) and the Saudi Building Code SBC 304 (2007) for superimposed dead and live loads of 2 and 3 kN/m^2, respectively. Table 1 shows the sizes and rebar detailing for both the prototype assembly and the test specimen. The column removal scenario considered in the experiments was decided on the basis of the risk assessment done for the prototype building (Figure 1), as presented in the next Section. Figure 2 shows the concrete dimensions of the specimen. The RC floor slab panels of the test specimen were cast monolithic with seven supporting RC beams B1-B7 and seven RC columns C1-C6. The RC columns were supported on steel stubs which were rigidly connected to steel rails anchored to the strong lab floor (Figure 3). The base of column C2 was removable for simulating a column loss scenario. This column will henceforth be called the 'test column'. The material properties of the steel rebars and concrete used in the test specimen are given in Table 2.

The column removal scenario of the building was replicated by removing the test column support and exerting a suddenly applied vertical load at the top of this column with the help of an actuator of 1000 kN peak load capacity.

Table 1. Geometric properties and reinforcement detailing of prototype building and test specimen.

Property	Prototype building	Specimen SMRF
Ground story height* (m)	6.75	1.69
Typical story height (m)	5	–
Beam span (m)	8	2
Beam width (mm)	800	200
Beam depth (mm)	800	200
Longitudinal rebars of beams	12ϕ20 (top) + 12ϕ20 (bottom)	2ϕ12 (top) + 2ϕ12 (bottom)
Beam stirrups at middle of span	ϕ12 @ 150 mm c/c (6 branches)	ϕ6 @ 100 mm c/c (2 branches)
Beam stirrups at end	ϕ12 @ 75 mm c/c (6 branches)	ϕ6 @ 50 mm c/c (2 branches)
Width of column section (mm)	800	200
Depth of column section (mm)	800	200
Longitudinal rebars of columns	20ϕ28	4ϕ16
Column ties	ϕ12 @ 75 mm c/c (at ends) ϕ12 @ 150 mm c/c (remaining)	ϕ6 @ 50 mm c/c (at ends) ϕ6 @ 100 mm c/c (remaining)
Clear concrete cover to transverse steel (mm)	40	10
Thickness of slab (mm)	240	60
Slab reinforcement in both ways	ϕ12 @ 150 mm c/c	ϕ6 @ 150 mm c/c

*Measured from top of footing to top of 1st floor level

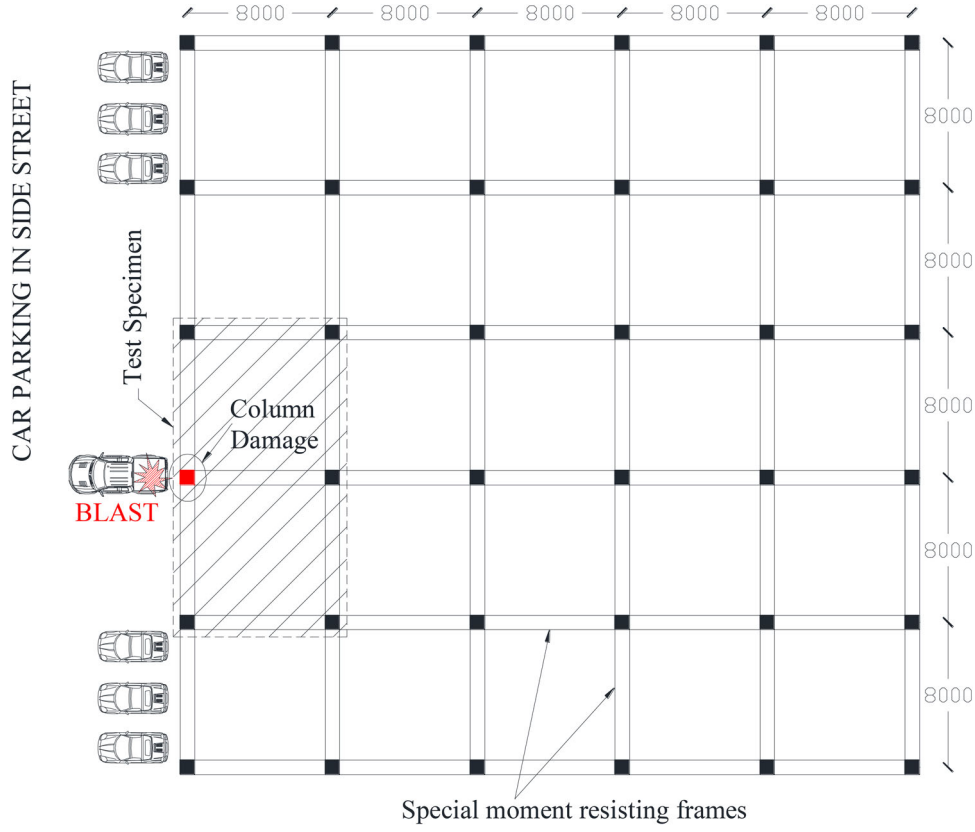

Figure 1. Layout plan of prototype RC framed building showing the damage of column of the test specimen extracted for testing (All dimensions are in mm).

The bases of all columns except the test column were fixed. Sand-filled jute bags were employed for applying a superimposed load of 5 kN/m^2 on the floor slab panels (Figure 3). The data was recorded at a speed of 1 k/s using a high-speed data acquisition system. The rebars of all beams and columns were instrumented using strain gages for recording the strains in the rebars. The vertical displacement of the test column and mid-span displacements of beams B1, B2 and B4 were measured using string potentiometers and laser transducers. Figure 3 depicts the instrumentation details of the specimen.

Figure 4 shows the displacement-time history applied through the actuator for testing the specimen. Strain rates of the order of 100–10,000 s^{-1} are reported in structures due to blast loads (Ngo, Mendis, Gupta, & Ramsay, 2007). However, the rate of loading was 100 mm/s, which was the maximum that could be applied using the actuator. Although the rate of application is on the lower side, the consequent reduction in inertial loads is partly compensated by the increase in the material strength on account of the strain rate effect. The recorded measurements were analysed to investigate the mechanism of progressive collapse.

3. Risk assessment

The quick assessment approach, developed earlier (Almusallam et al., 2016) based on FEMA 426 (2003), was employed for the blast risk assessment of the prototype

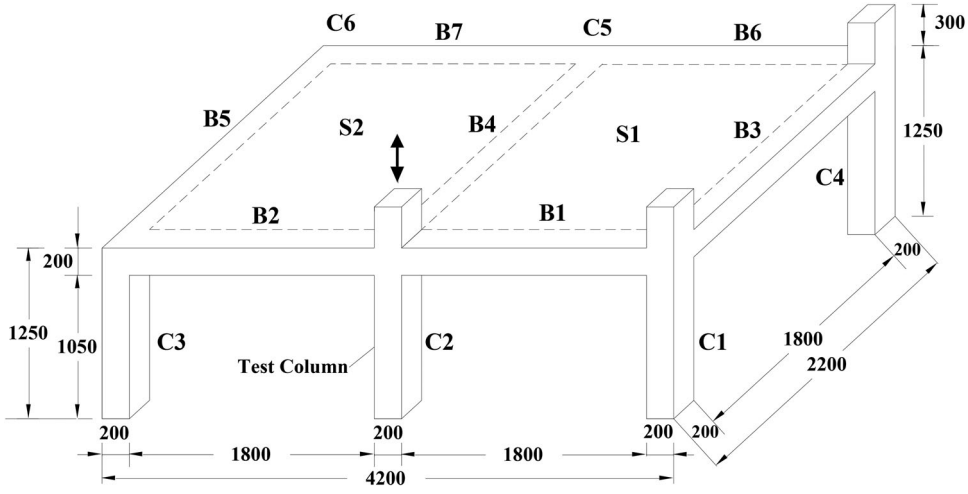

Figure 2. Concrete dimensions of test specimen SMRF.

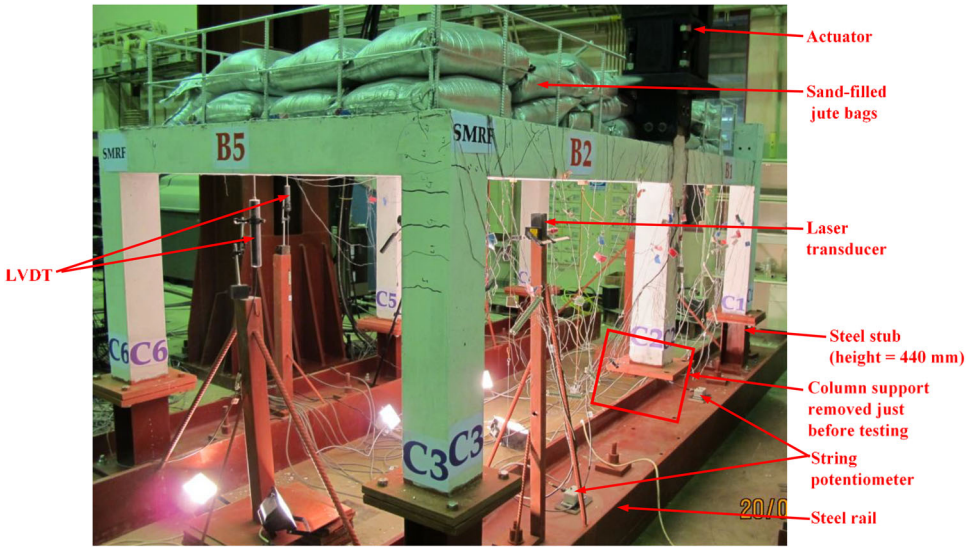

Figure 3. Instrumentation layout for specimen SMRF.

Table 2. Material properties used in the FE modeling.

Concrete			
Material model		Type 159 (MAT_CSCM_CONCRETE)	
Density (kg/m^3)		2320	
Uniaxial compressive strength (MPa)		57.3	
Erosion factor		1.05	
Maximum aggregate size (mm)		10.0	
Steel rebars	ϕ6	ϕ12	ϕ16
Material model		Type 24 (MAT_PIECEWISE_LINEAR_PLASTICITY)	
Density (kg/m^3)		7850	
Young's modulus (GPa)		200	
Poisson's ratio		0.3	
Strain rate parameter, *C*		250	
Strain rate parameter, *p*		1.6	
Yield stress (MPa)	290	588	588
Tangent modulus (MPa)	388	660	660
Plastic strain to failure (%)	19.8	14.7	14.7
Steel stubs at base of columns			
Material model		Type 1 (MAT_ELASTIC)	
Density (kg/m^3)		7850	
Young's modulus (GPa)		200	
Poisson's ratio		0.3	

building (Figure 1). The risk is associated with the threat/hazard level, vulnerability (probability of failure) assessment, and consequence or asset value assessment. The assessment of threat considers the possibilities of attack of different

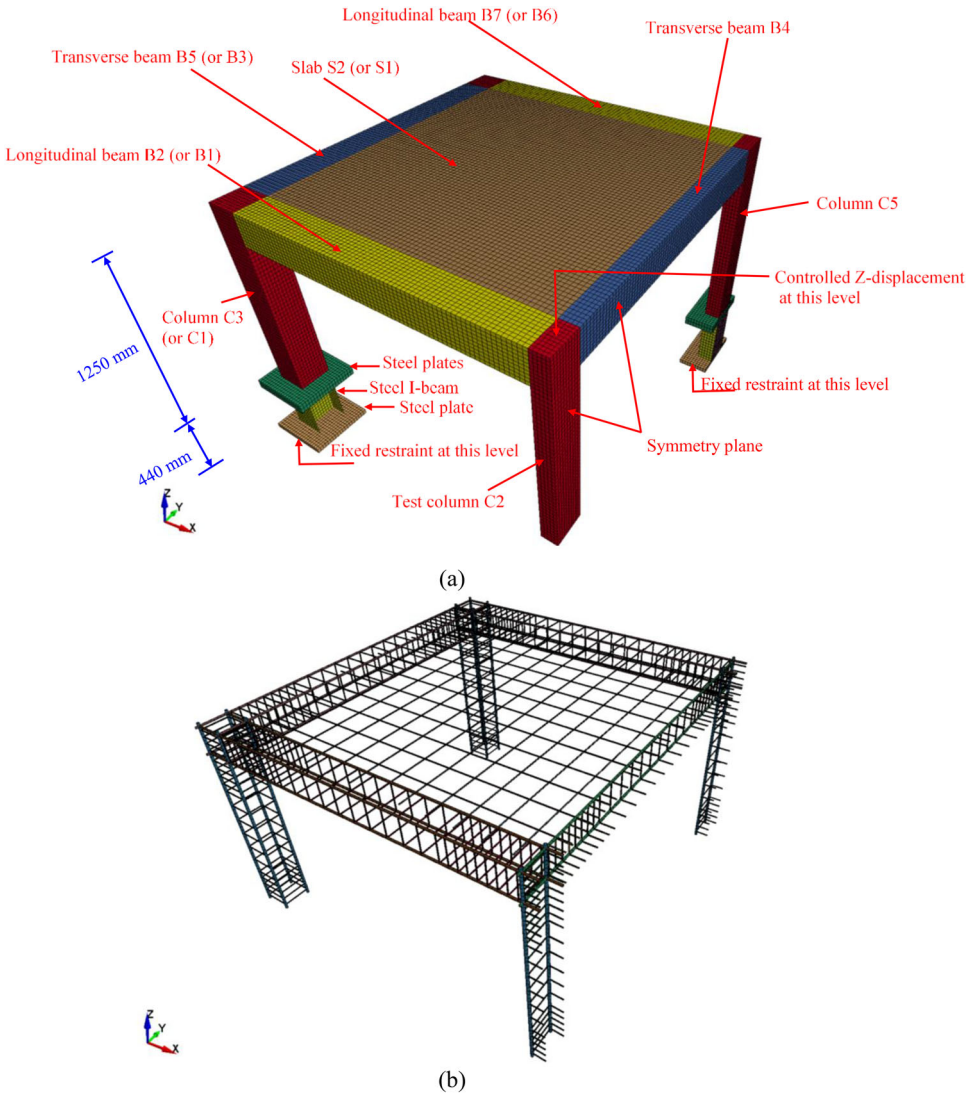

Figure 4. FE model for specimen SMRF: (a) One-half of specimen; (b) Steel reinforcement for one-half of specimen.

Table 3. Vulnerability and consequence level ratings.

S.N.	Factors	Level*	Prototype building	
			Level	Comment
		Vulnerability		
1	Asset visibility	1-4	4	Well known building located in dense, urban area on busy intersection
2	Building significance	1-4	2	Office building
3	Critical element accessibility	1-4	4	Exposed critical columns, street-side parking with no stand-off
4	Critical element vulnerability	1-4	2	Medium sized RC building
5	Structural system characteristics	1-4	2	Concrete moment-resisting frames
	Total =	1-20	14	
	Rating: 1 – 5 = Low (=1) 6 – 10 = Medium (=2) 11 – 15 = High (=3) 16 – 20 = Very High (=4)			**Rating**: High (i.e. 3)
		Consequence		
1	Injuries/fatalities level	1-10	6	Low rise structure with more dominant horizontal footprint than height
2	Impact of suspended activities	1-10	5	Non-critical infrastructure
	Total = **Rating**: Same as above	1-20	11	**Rating**: High (i.e. 3)

*Level 1 represents the lowest risk

nature and methods. It is usually difficult to precisely foresee the likelihood of an attack and thus possible credible threat scenarios need to be assessed. As the building is located in dense, urban area, with street-side parking, major threat to the building is from blast in an explosive laden vehicle parked close the building causing column loss

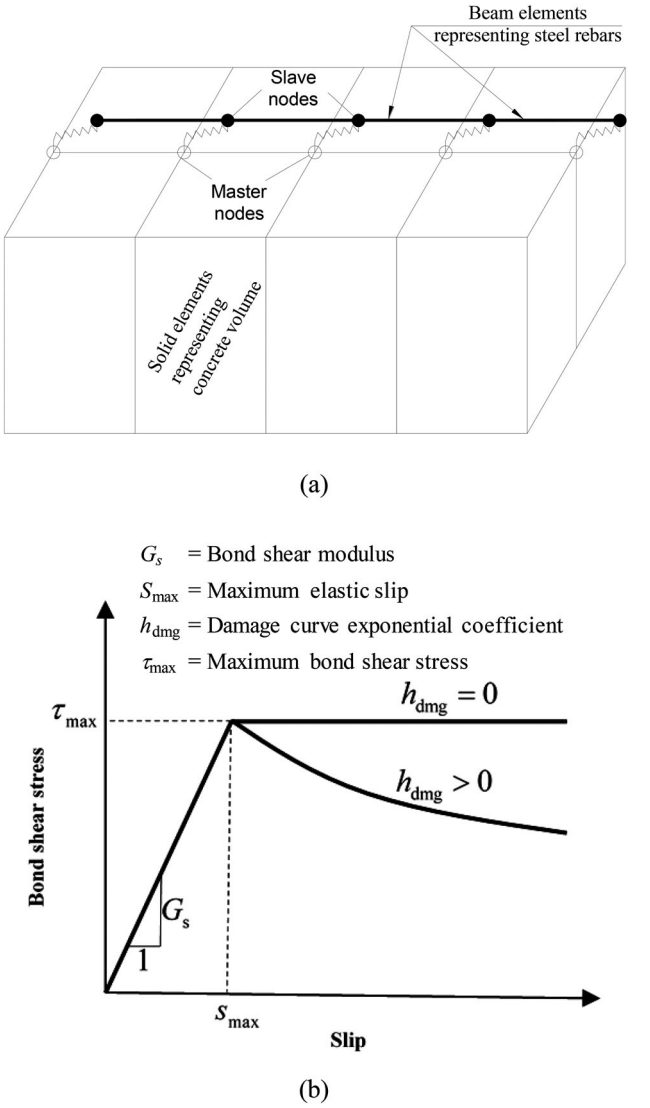

Figure 5. Bond-slip modeling at concrete-to-steel rebars interface: (a) Sketch of fictitious springs between master and slave nodes in 1-D slide line model; (b) Bond shear stress versus slip curve.

(Figure 1). Assuming the threat level to be constant the conditional risk is assessed based on vulnerability and consequence rating for which Table 3 is used (Almusallam et al., 2016). The two ratings are then employed to estimate the conditional risk from the following relation:

$$\text{Conditionalrisk rating} = \text{Vulnerability rating} + \text{Consequence rating} - 1 \quad (1)$$

The vulnerability and consequence ratings vary from 1 to 4 depending on the rating varying from Low to Very high (1 for Low, 2 for Medium, 3 for High, and 4 for Very high), as shown in Table 3. Thus the conditional risk rating varies from one to seven with larger the number, greater is the risk to damage. The vulnerability and consequence ratings for the prototype building are given in Table 3. The vulnerability and consequence ratings for the prototype building are High (=3). Thus, the conditional risk rating of the building using Equation (1) is 5, which indicates that there is a high risk of column-loss in the prototype building.

4. FE modelling

The high-fidelity FE software LS-DYNA (2007) was employed to perform FE simulations of the test specimen. Half of the specimen was only modelled due to symmetry (Figure 4(a)). The concrete volume of the beams, columns, and slabs was meshed using eight-node solid hexahedron elements of reduced integration. Figure 4(b) displays the FE model of the steel reinforcement for half of the specimen. Hughes-Liu beam elements were employed for modelling of the steel rebars. Eight node solid and Belytschko-Tsay shell elements (Belytschko, Lin, & Chen-Shyh, 1984) were employed for modelling of the steel stubs at the column (Figure 4(a)). The size of concrete and steel rebar elements in the model ranged from 20 to 30 mm, which was decided based on a mesh sensitivity test.

The concrete was modelled by employing the continuous surface cap model (type 159) together with the erosion. Concrete elements were allowed to erode when the maximum principal strain exceeded 0.05 (Murray, Abu-Odeh, & Bligh, 2007). The elasto-plastic material model (type 24) was used for modelling steel rebars. The model of type 1 (linear elastic) was used to model the steel stubs thereby assuming linear elastic material behaviour. Table 2 summarizes the material properties employed in the FE modelling.

In this study, perfect bond was assumed between concrete and the rebars (flexural and shear) of columns C1 to C6, the transverse rebars of all beams B1 to B7, and steel rebars of beams B3, B5, B6, and B7. However, bond-slip effects were considered between the concrete and main rebars of beams B1, B2, and B4 and between the slab rebars and concrete. The bond-slip effect was simulated by using a 1-D contact interface between the solid and beam elements representing the concrete and rebars, respectively, through fictitious springs, as shown in Figure 5(a) (LS-DYNA, 2007).

The bond shear stress-slip formulation for the 1-D slide line model, employed in the study, is depicted in Figure 5(b), which is given by:

$$\tau = \begin{cases} G_s s & s \le s_{max} \\ \tau_{max} e^{-h_{dmg} D} & s > s_{max} \end{cases} \quad (2)$$

where D is the damage parameter (defined as the algebraic sum of the absolute values of the plastic displacement increment); G_s is the bond shear modulus; h_{dmg} is the damage curve exponential coefficient; and s_{max} is the maximum elastic slip. The material parameters required for the use of one-dimensional slide-line model in LS-DYNA are: the bond shear modulus G_s, the maximum elastic slip s_{max}, and the damage curve exponential coefficient h_{dmg}. In this research, the maximum elastic slip was taken equal to 0.254 mm, as recommended by Xiao and Rui (1997), and the maximum bond stress τ_{max} was assumed as $1.9 f_t$ (de Witte, 2005), where f_t is the tensile strength of concrete $= 0.62\sqrt{f'_c}$ (where f'_c = cylinder strength of concrete in MPa). Hence, the bond shear modulus G_s was assumed as:

$$G_s = \frac{1.9 \times 0.62\sqrt{f'_c}}{0.254} = 4.64\sqrt{f'_c} \quad \text{(MPa units)} \quad (3)$$

The value of h_{dmg}, was taken as a variable, as will be discussed in Section 4.

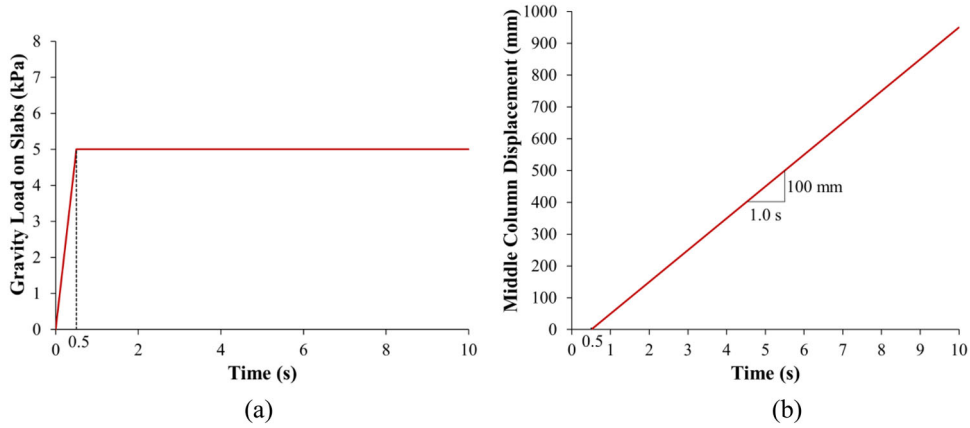

Figure 6. Load application for FE model of specimen SMRF: (a) Gravity load on slabs; (b) Prescribed vertical displacement at location of middle column C2.

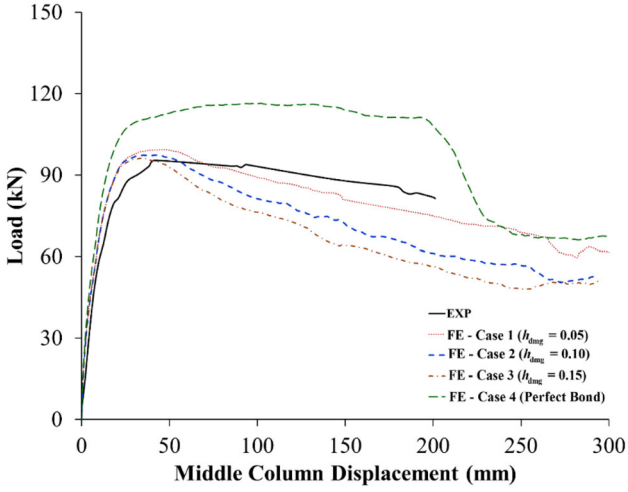

Figure 7. Experimental and FE load-displacement envelopes for specimen SMRF.

The displacements and rotations of the base of the steel stubs were restrained (Figure 4(a)). Symmetric boundary conditions were implemented for nodes on the plane of symmetry. The superimposed gravity load on the slabs was modelled as a uniform load acting in the negative Z-direction as a ramp function, increasing from zero at the onset of the analysis to its peak value of 5.0 kPa at a time of 0.5 s, and then held constant for the remainder of the analysis time (Figure 6(a)). This was done to eliminate the oscillatory response associated with the dynamic analysis. The displacement-time history was simulated at the top nodes of the test column using Figure 6(b). This prescribed displacement-controlled loading was assumed to start at a time of 0.5 s at which the gravity load reached its peak value (Figure 6(b)). To simulate the experiment, the rate of increase of the downward displacement was taken as 100 mm/s (see Figure 6(b)).

Yu, Rinder, Stolz, Tan, and Riedel (2014) showed that for buildings exposed to blast loads, the strain rate in steel rebars varies from 0.01 to 0.1 s^{-1}. The strain rate in rebars in our similar experiments (Al-Salloum et al., 2018) was found to be 0.01 s^{-1}, which was obtained from the experimental testing of three RC frame test specimens as an average value of strain versus time recording. Thus the strain rate in rebars corresponding to the applied rate of loading conforms with the findings of Yu et al. (2014).

5. Validation of numerical modeling

The experimental test results for the SMRF specimen were employed to validate the FE model and the results of numerical analysis procedure, which are discussed hereafter. As outlined previously, bond-slip effects between the concrete and main steel rebars of the beams (B1, B2, and B4) and slabs (S1 and S2) were considered in the FE model, and the value of h_{dmg} was varied from 0.05 to 0.15. Four different FE models were then created for specimen SMRF. The first case is for bond-slip effects with $h_{dmg} = 0.05$. The second and third cases are for curve exponential coefficient (h_{dmg}) of 0.10 and 0.15, respectively. The last case (case 4) is for the analysis with a perfect bonding assumption between all reinforcing rebars and concrete, to be taken as an upper bound solution.

Figure 7 presents a comparison between the numerical and experimental load-displacement variations. It is observed from Figure 7 that the FE model with the perfect bonding assumption (case 4) significantly overestimated the stiffness as well as the peak load with a ratio of the predicted to tested peak load of 1.22. The FE model of cases 2 and 3 significantly underestimated the post peak load slope of the load-displacement curve. Nevertheless, the FE model of case 1 closely conforms to the test results in terms of the load-displacement curve. Thus, the bond-slip model with the value of h_{dmg} as 0.05 was considered successful in predicting the load-displacement characteristics the SMRF specimen. Figure 7 depicts that the experimental load-displacement curve did not continue beyond a middle column displacement of about 200 mm because the test was stopped due to the limitation of the actuator stroke.

Figure 8 illustrates the experimental failure modes for the frames of the SMRF specimen as compared to the predicted failure modes. The failure modes observed in the FE model are depicted in Figure 8 using damage contours (effective plastic strain) ranging from 0 to 1, with 0 indicating no damage and 1 designating full damage. It is worth mentioning here that the experimental modes of failure shown in

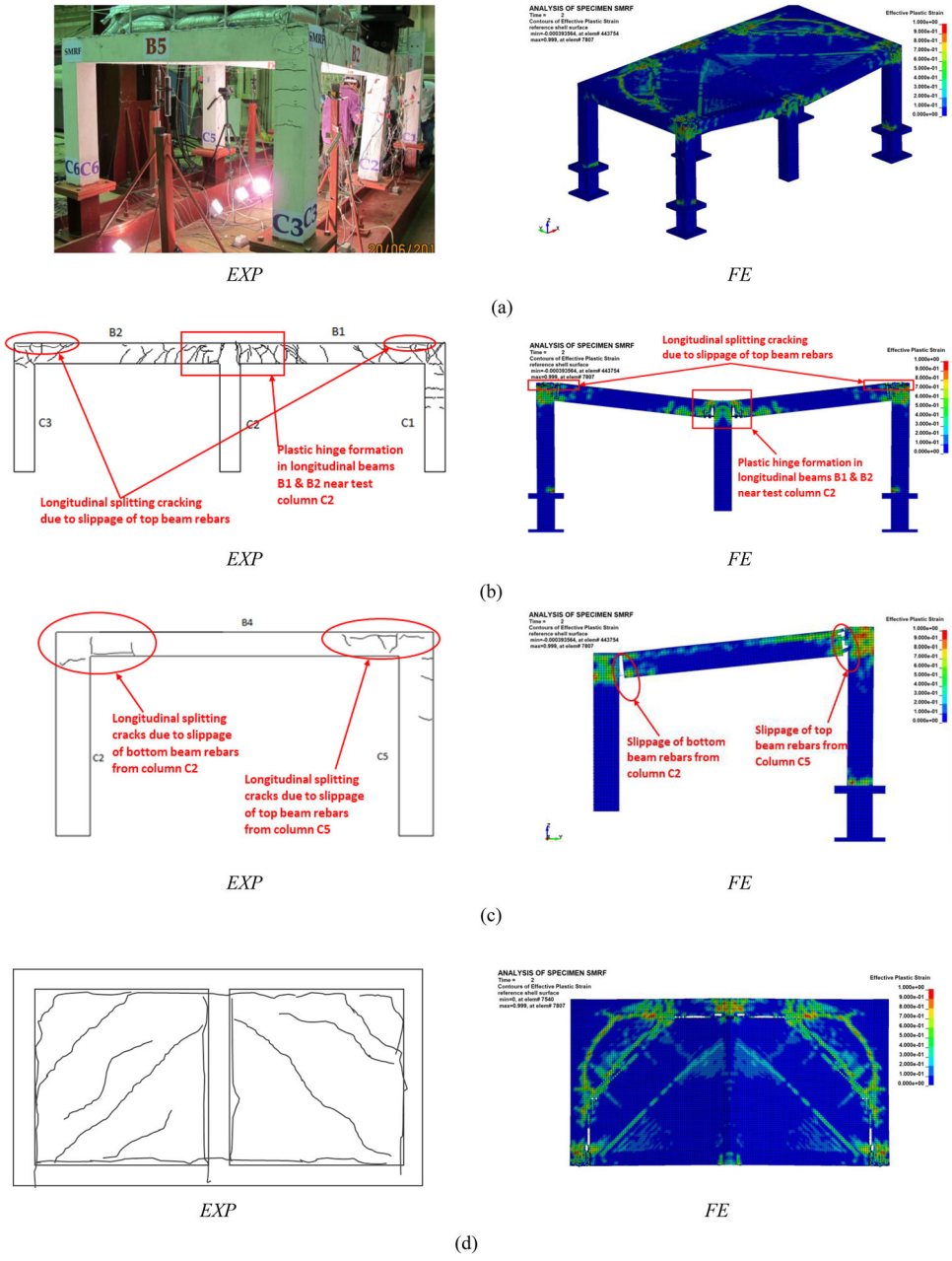

Figure 8. Comparison of experimental and FE mode of failure of frames of specimen SMRF: (a) Whole specimen; (b) Longitudinal frame containing test column C2; (c) Transverse frame containing test column C2; (d) Top view of slabs.

Figure 8 were corresponding to the end of the test (at a middle column displacement of about 200 mm) and the FE failure modes are presented at the same displacement for the purpose of making comparison. Because of the limitations of the smeared crack approach, whereby the cracks are distributed over the elements rather than isolated, the comparison between the experimental crack pattern and the damage parameter contours of the FE model does not show a precise correlation. The damage parameter appears to be spread over a wider area of damage because the smeared crack approach smears the hairline cracks, which may not be visible in the tests.

Nevertheless, the damage parameter contours of FE model tend to predict of crack growth reasonably well (Figure 8). As illustrated in Figure 8, considerable damage was observed in both slab panels, longitudinal beams B1 and B2, and transverse beam B4. Columns C1, C2, C3, and C4 were lightly damaged. However, columns C5 and C6, longitudinal beams B6 and B7 and transverse beams B3 and B5 were almost undamaged. Figures 8(a) and (b) show that the plastic hinges were formed in the longitudinal beams B1 and B2 near one of their connections with the middle column, which is characterized by wide flexural cracks and the crushing of concrete in compression (Figure 8(b)).

However, at the exterior joints (near columns C1 and C3), plastic hinge was not formed in the beam due to partial slippage of the top beam rebars in the joint region, which can be evidenced from the longitudinal splitting cracks at the exterior joints (Figure 8(b)). For the transverse frame containing the test column, slippage was also noticed between the bottom rebars of beam B4 and test column C2, and between the top rebars of beam B4 and outer column C5, as seen in

Table 4. Comparison of key experimental and FE results for test specimen SMRF*.

Results	P_y (kN)	P_u (kN)	Δ_y (mm)	$\Delta_{u,c}$ (mm)	Δ_u (mm)	$\Delta_{u,B1,2}$ (mm)	$\Delta_{u,B4}$ (mm)	$\Delta_{u,s}$ (mm)	E_u (kNm)	$\varepsilon_{sb,B1,2}$ (με)	$\varepsilon_{st,B1,2}$ (με)	$\varepsilon_{st,B4}$ (με)
EXP	NA	95.4	NA	41.5	200.6	91.3	87.3	54.8	17.4	NA	2411	2935
FE	73.9	99.4	12.0	45.0	182.6	91.1	96.0	53.6	15.7	***144744***	2386	2744
EXP/FE	–	0.96	–	0.92	1.10	1.00	0.91	1.02	1.10	–	1.01	1.07

*P_y = load at first yield of bottom steel rebars of longitudinal beams B1 & B2 at inner column face; P_u = peak load; Δ_y = displacement of middle column C2 at first yield of bottom steel rebars of longitudinal beams B1 & B2; $\Delta_{u,c}$ = displacement of middle column C2 at peak load; Δ_u = displacement of middle column C2 at ultimate state; $\Delta_{u,B1,2}$ = mid-span displacement of longitudinal beams B1 & B2 at ultimate state; $\Delta_{u,B4}$ = mid-span displacement of transverse beam B4 at ultimate state; $\Delta_{u,s}$ = mid-span displacement of slabs S1 & S2 at ultimate state; E_u = energy dissipated at ultimate state; $\varepsilon_{sb,B1,2}$ = strain of bottom steel rebars of longitudinal beams B1 & B2 at inner column face (C2); $\varepsilon_{st,B1,2}$ = strain of top steel rebars of longitudinal beams B1 & B2 at outer column face (C1 or C3); $\varepsilon_{st,B4}$ = strain of top steel rebars of transverse beam B4 at outer column face (C5); EXP = experimental; FE = finite element; NA = not available data; strain values in italic bold font exceed their respective yield strains.

Table 5. Details of FE matrix used in the parametric study*.

Specimen	α_s	Type of assembly	Existence of slabs	Full development of longitudinal rebars of beams B1 & B2 at outer columns C1 and C3	No. of column stories	No. of spans	Depth of columns C1 and C3 (mm)	Axial load ratio on top of columns C1 and C3
Specimens with different assembly type								
SMRF	1.3	3D	Yes	No	1	2	200	0
SMRF-NS	1.3	3D	No	No	1	2	200	0
SMRF-2D	1.3	2D	No	No	1	2	200	0
Specimens with 2D assemblies								
SMRF-2D-FDBR-0.0	1.3	2D	No	Yes	1	2	200	0
SMRF-2D-FDBR-0.18	1.3	2D	No	Yes	1	2	200	0.18
SMRF-2D-FDBR-0.30	1.3	2D	No	Yes	1	2	200	0.3
SMRF-2D-FDBR-0.40	1.3	2D	No	Yes	1	2	200	0.4
SMRF-2D-FDBR-CC-0.0	2.9	2D	No	Yes	2	2	200	0
SMRF-2D-FDBR-CC-0.18	2.9	2D	No	Yes	2	2	200	0.18
SMRF-2D-FDBR-CC-0.30	2.9	2D	No	Yes	2	2	200	0.3
SMRF-2D-FDBR-CC-0.40	2.9	2D	No	Yes	2	2	200	0.4
SMRF-2D-FDBR-CC-BC-0.0	3.9	2D	No	Yes	2	4	200	0
SMRF-2D-FDBR-CC-BC-0.18	3.9	2D	No	Yes	2	4	200	0.18
SMRF-2D-FDBR-CC-BC-0.30	3.9	2D	No	Yes	2	4	200	0.3
SMRF-2D-FDBR-CC-BC-0.40	3.9	2D	No	Yes	2	4	200	0.4
SMRF-2D-FDBR-CC-BC-SC1-0.0	11.8	2D	No	Yes	2	4	300	0
SMRF-2D-FDBR-CC-BC-SC1-0.18	11.8	2D	No	Yes	2	4	300	0.18
SMRF-2D-FDBR-CC-BC-SC1-0.30	11.8	2D	No	Yes	2	4	300	0.3
SMRF-2D-FDBR-CC-BC-SC1-0.40	11.8	2D	No	Yes	2	4	300	0.4
SMRF-2D-FDBR-CC-BC-SC2-0.0	23.9	2D	No	Yes	2	4	400	0
SMRF-2D-FDBR-CC-BC-SC2-0.18	23.9	2D	No	Yes	2	4	400	0.18
SMRF-2D-FDBR-CC-BC-SC2-0.30	23.9	2D	No	Yes	2	4	400	0.3
SMRF-2D-FDBR-CC-BC-SC2-0.40	23.9	2D	No	Yes	2	4	400	0.4
SMRF-2D-FDBR-CC-BC-SC3-0.0	78.2	2D	No	Yes	2	4	600	0
SMRF-2D-FDBR-CC-BC-SC3-0.18	78.2	2D	No	Yes	2	4	600	0.18
SMRF-2D-FDBR-CC-BC-SC3-0.30	78.2	2D	No	Yes	2	4	600	0.3
SMRF-2D-FDBR-CC-BC-SC3-0.40	78.2	2D	No	Yes	2	4	600	0.4

*For two-story specimens, top 200 mm of second-story columns are restrained against translation in X & Y and against rotation about X, Y & Z directions.

Figure 8(c). Slippage of the rebars in beams B1, B2, and B4 at the exterior joints can be explained as follows:

According to Sec. 12.5 of the ACI 318-11 code (2011), the tensile development length of the deformed rebars terminating in a standard hook (ℓ_{dh}) shall not be less than the largest of $0.24f_y/\sqrt{f'_c}d_b$, $8d_b$, and 150 mm, where f_y = yield strength of rebars (in MPa); f'_c = cylinder compressive strength of concrete (in MPa); and d_b = rebar diameter (in mm). Thus, for the prototype building, ℓ_{dh} was calculated as 373 mm (for ϕ20 mm rebars) and the available distance for anchorage inside the outer columns was 720 mm, which will provide full development of the beam rebars. Nevertheless, for the model scale assembly (specimen SMRF), ℓ_{dh} was calculated as 224 mm (for ϕ12 mm rebars) and the available distance for anchorage inside the outer columns was only 168 mm, which will not provide full development of stress in beam rebars. Accordingly, slip of the beam rebars was found at the exterior joints, as discussed above.

The key experimental and FE results for the SMRF specimen are compared in Table 4. It is worth mentioning here that the ultimate state, adopted here, is defined as the state at which the load drops to 0.8 P_u, where P_u is the peak load (NZS 4203, 1992). Table 4 shows a deviation of 4% in the prediction of peak load. However, compared with the test results, deviations of 8%, 10%, 0%, 9% and 2% were found for the test column displacement at peak load, test column displacement at the ultimate state, mid-span displacement of beams B1 and B2 at ultimate conditions, mid-span displacement of beam B4 at the ultimate state, and mid-span displacement of slabs at the ultimate state, respectively. It is explicable from Table 4 that the dissipated energy at ultimate conditions (area under the load-displacement curve up to the ultimate displacement Δ_u) is close to the FE model results, with a deviation of 10%.

Table 4 also presents the strains in longitudinal rebars of beams B1, B2, and B4 obtained numerically and

Table 6. Summary of FE results for all specimens*.

				Flexural action stage			Compressive arch action stage				Catenary action stage								
Specimen ID	α_s	P_y (kN)	Δ_y (mm)	$P_{u,FA}$ (kN)	$\Delta_{u,c\text{-}FA}$ (mm)	$N_{u,FA}$ (kN)	Development	$P_{u,CAA}$ (kN)	$\Delta_{u,c\text{-}CAA}$ (mm)	$N_{u,CAA}$ (kN)	Development	$P_{u,CA}$ (kN)	$\Delta_{u,c\text{-}CA}$ (mm)	$N_{u,CA}$ (kN)	$\varepsilon_{b,u}$ ($\mu\varepsilon$)	$\varepsilon_{t,u}$ ($\mu\varepsilon$)	Δ_u (mm)	E_u (kN.m)	P_u (kN)
Specimens with different assembly type																			
SMRF	1.3	74	12	99	45	−28	N	–	–	–	N	–	–	–	***144744***	2386	183	16	99
SMRF-NS	1.3	55	13	72	29	−22	N	–	–	–	N	–	–	–	***139136***	2345	105	6	72
SMRF-2D	1.3	36	14	41	38	−16	N	–	–	–	N	–	–	–	***138351***	1673	100	4	41
Specimens with 2D assemblies																			
SMRF-2D-FDBR-0.0	1.3	41	14	48	24	−24	N	–	–	–	N	–	–	–	***222133***	2522	692	27	48
SMRF-2D-FDBR-0.18	1.3	52	14	66	88	−36	N	–	–	–	N	–	–	–	***217943***	***180151***	562	31	66
SMRF-2D-FDBR-0.30	1.3	56	14	71	89	−33	N	–	–	–	P	89	647	74	***208128***	***193279***	653	41	89
SMRF-2D-FDBR-0.40	1.3	59	16	71	127	−33	N	–	–	–	P	84	629	70	***227624***	***178066***	700	45	84
SMRF-2D-FDBR-CC-0.0	2.9	41	13	62	95	−74	N	–	–	–	P	90	504	110	***225307***	***173275***	607	42	90
SMRF-2D-FDBR-CC-0.18	2.9	55	14	78	71	−130	N	–	–	–	P	134	506	206	***230002***	***173367***	533	46	134
SMRF-2D-FDBR-CC-0.30	2.9	60	14	85	67	−149	N	–	–	–	P	141	480	224	***221115***	***171643***	550	51	141
SMRF-2D-FDBR-CC-0.40	2.9	66	17	86	65	−157	N	–	–	–	P	137	458	225	***182035***	***184216***	499	45	137
SMRF-2D-FDBR-CC-BC-0.0	3.9	51	14	72	61	−164	N	–	–	–	F	241	829	269	***223695***	***226319***	833	104	241
SMRF-2D-FDBR-CC-BC-0.18	3.9	64	15	89	42	−160	Y	83	95	−241	F	256	835	275	***223544***	***213131***	839	118	256
SMRF-2D-FDBR-CC-BC-0.30	3.9	68	15	94	66	−212	Y	93	78	−261	F	295	963	275	***220300***	***180342***	967	157	295
SMRF-2D-FDBR-CC-BC-0.40	3.9	72	17	95	54	−190	Y	93	77	−266	F	200	615	276	***214807***	***178655***	621	71	200
SMRF-2D-FDBR-CC-BC-SC1-0.0	11.8	63	15	85	54	−225	Y	84	56	−310	F	250	829	274	***221128***	***226115***	838	111	250
SMRF-2D-FDBR-CC-BC-SC1-0.18	11.8	74	15	97	29	−229	Y	104	51	−438	F	285	939	273	***221167***	***215708***	949	148	285
SMRF-2D-FDBR-CC-BC-SC1-0.30	11.8	77	15	101	29	−229	Y	111	53	−462	F	289	948	274	***221391***	***223321***	949	152	289
SMRF-2D-FDBR-CC-BC-SC1-0.40	11.8	79	15	103	29	−229	Y	114	59	−472	F	292	949	273	***223868***	***228752***	949	154	292
SMRF-2D-FDBR-CC-BC-SC2-0.0	23.9	74	15	94	29	−229	Y	99	55	−439	F	275	900	272	***222908***	***237501***	908	134	275
SMRF-2D-FDBR-CC-BC-SC2-0.18	23.9	86	15	102	20	−229	Y	123	45	−538	F	294	949	274	***218502***	***225818***	949	154	294
SMRF-2D-FDBR-CC-BC-SC2-0.30	23.9	89	15	106	20	−229	Y	130	47	−559	F	299	949	273	***222633***	***232124***	949	158	299
SMRF-2D-FDBR-CC-BC-SC2-0.40	23.9	92	15	109	20	−229	Y	133	48	−571	F	291	906	272	***223841***	***244176***	910	149	291
SMRF-2D-FDBR-CC-BC-SC3-0.0	78.2	92	14	92	14	−229	Y	131	39	−615	F	278	859	272	***213942***	***232817***	877	135	278
SMRF-2D-FDBR-CC-BC-SC3-0.18	78.2	112	15	95	12	−229	Y	147	36	−667	F	283	839	274	***216150***	***234452***	843	134	283
SMRF-2D-FDBR-CC-BC-SC3-0.30	78.2	116	15	100	12	−229	Y	155	33	−693	F	287	839	272	***215980***	***233762***	854	141	287
SMRF-2D-FDBR-CC-BC-SC3-0.40	78.2	120	15	103	12	−229	Y	159	33	−691	F	289	839	271	***208159***	***227625***	845	141	289

*P = partially developed; N = not developed; F = fully developed; P_y = load at first yield of bottom steel rebars of longitudinal beams B1 & B2 at inner column face; Δ_y = displacement of middle column C2 at first yield of bottom steel rebars of longitudinal beams B1 & B2; $P_{u,FA}$ = peak load of flexural action stage; $\Delta_{u,c\text{-}FA}$ = displacement of middle column C2 at peak load of flexural action stage; $N_{u,FA}$ = peak axial force of beam B1 (or B2) at flexural action stage (+ve is tension); $P_{u,CAA}$ = peak load of compressive arch action stage; $\Delta_{u,c\text{-}CAA}$ = displacement of middle column C2 at peak load of compressive arch action stage; $N_{u,CAA}$ = peak axial force o beam B1 (or B2) at compressive arch action stage (+ve is tension); $P_{u,CA}$ = peak load of catenary action stage; $\Delta_{u,c\text{-}CA}$ = displacement of middle column C2 at peak load of catenary action stage; $N_{u,CA}$ = peak axial force of beam B1 (or B2) at catenary action stage (+ve is tension); $\varepsilon_{b,u}$ = strain of bottom steel rebars of longitudinal beams B1 & B2 at inner column face at ultimate state; $\varepsilon_{t,u}$ = strain of top steel rebars of longitudinal beams B1 & B2 at outer column face at ultimate state; Δ_u = displacement of middle column C2 at ultimate state; E_u = energy dissipated at ultimate state; P_u = progressive collapse resistance = maximum of $P_{u,FA}$, $P_{u,CAA}$ and $P_{u,CA}$; strain values in italic bold font exceed their respect

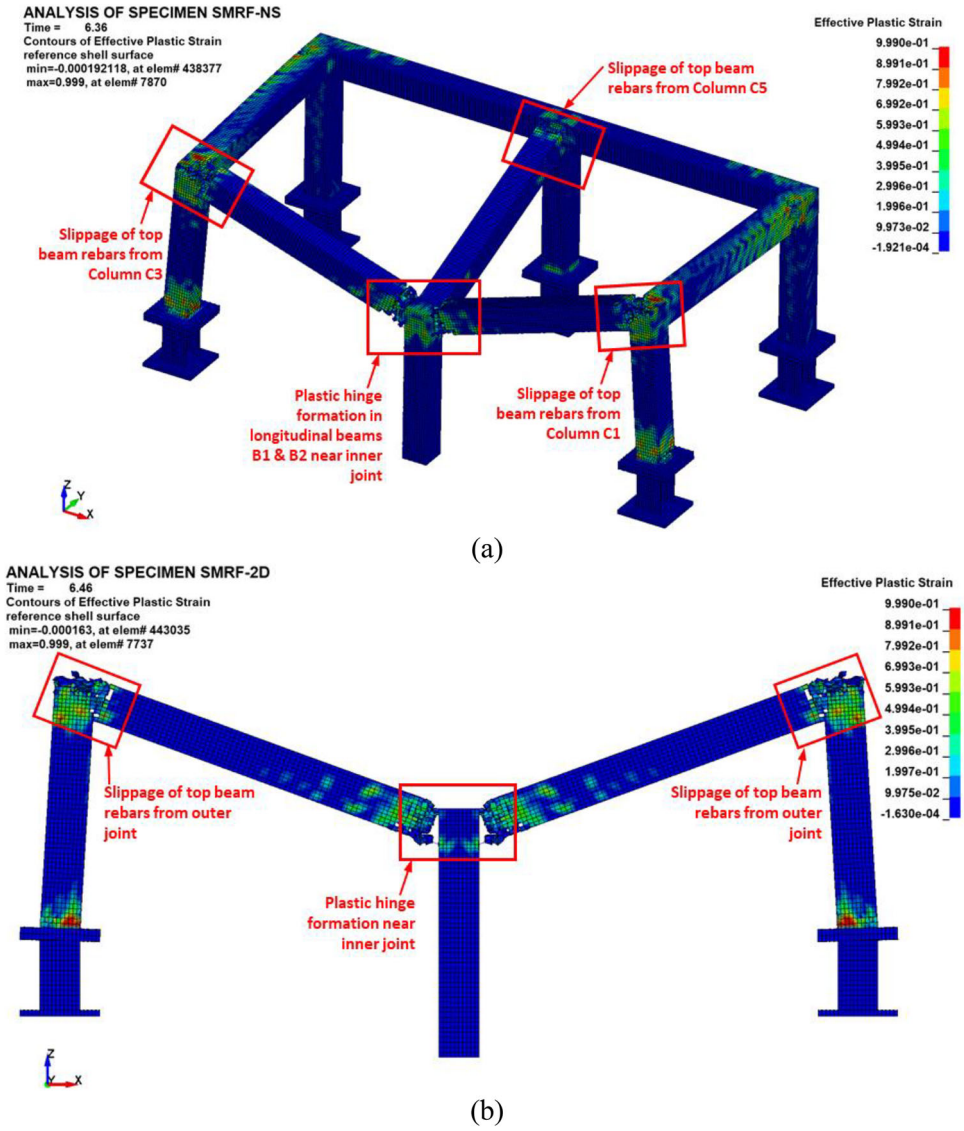

Figure 9. FE mode of failure for specimens: (a) SMRF-NS; (b) SMRF-2D.

experimentally for the SMRF specimen at the ultimate state. The numerical and experimental values show good agreement. It is evident from Table 4 that the predicted peak strain for the bottom rebars of the longitudinal beams B1 and B2 at the inner column face was about 49 times the rebar yield strain, which shows the full formation of plastic hinges, as discussed above. However, both experimental and predicted peak strains for the top rebars of longitudinal beams B1 and B2 at the face of the exterior columns C1 and C3 were less than the rebar yield strain due to the insufficient development length available for the top rebars at the exterior joints, which caused rebar slippage as discussed earlier. The same behaviour was found for the top rebars of the transverse beam B4 at the face of column C5.

It is worth mentioning here that the developed FE model captured the severe damage distribution near test column C2, as well as at the beam-column joints in the adjacent columns (Figure 8). These are major mechanisms that are activated in the event of progressive collapse. Other damage effects such as fracture of steel rebars or catenary/membrane actions were not observed in the test specimen SMRF. However, the same FE model was capable of simulating fracture of longitudinal beam rebars of another precast RC beam-column frame tested previously by the authors under column-loss scenario in a separate study (Elsanadedy et al. 2017). In short, validity of the conducted FE modeling is justified and hence, the numerical models can be extended for parametric studies of practical interest.

6. Parametric study

6.1. Effect of assembly type

The calibrated FE model detailed previously in Sec. 3 was employed to study the effect of the assembly type on the response of RC SMRF under column-removal scenario. The investigated configurations included a 3D assembly with slabs (specimen SMRF), 3D assembly without slabs (specimen SMRF-NS), and 2D assembly (specimen SMRF-2D), as shown in Table 5. The acronyms 'NS' and '2D' in the designation of these specimens, represents no slab and 2D assembly, respectively. The SMRF-NS specimen is generally the same as the SMRF

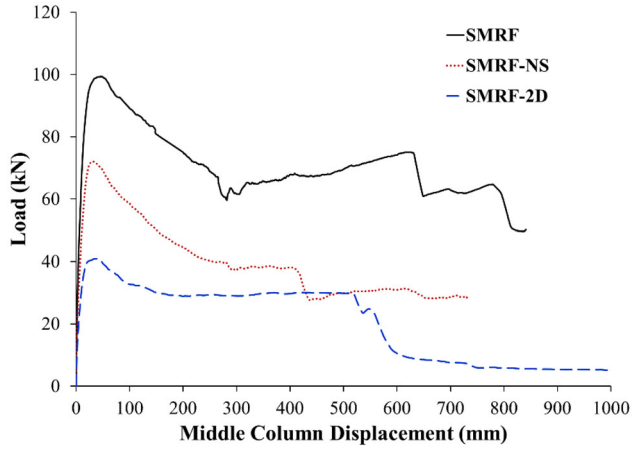

Figure 10. Load-displacement envelopes for specimens with different assembly type.

specimen but with the removal of slab panels S1 and S2. However, the SMRF-2D specimen is a 2D assembly comprising of beams B1 and B2 in addition to columns C1, C2, and C3. The results of analysis of the three specimens are summarized in Table 6 in terms of all the response parameters at different action stages and ultimate conditions. The FE modes of failure for specimens SMRF-NS and SMRF-2D are also shown in Figure 9.

Figure 10 depicts a comparison between the numerical and experimental load versus the middle column displacement envelopes for the three specimens. It is clear that neither a compressive arch action nor catenary action could be developed in the three specimens due to the insufficient restraint provided by the outer columns, and also because of the inadequate tension development length available for the top beam rebars inside the exterior joints. This was also evidenced from the peak axial forces of beam B1 (or B2) given in Table 6 for the three specimens, which were very small (approximately equal to zero). Flexural action was only developed at the inner beam-column joints of beams B1 and B2 via plastic hinge formation. However, it could not be developed at the exterior joints because of rebar slippage as depicted from the strains reported in Table 6 for the top beam rebars, which were quite less than their respective yield value.

Table 6 and Figure 10 also indicate that removing the slab panels S1 and S2 from the FE model of specimen SMRF reduced the peak load capacity of the assembly by about 27%. In addition, removing all of the slab panels S1 and S2; columns C4, C5 and C6; transverse beams B3, B4 and B5; and longitudinal beams B6 and B7 from the FE model of the SMRF specimen caused reduction in the peak load capacity by about 59%. Therefore, it can be discerned that modelling RC slabs in the 3D assemblies increased the flexural action capacity and the progressive collapse resistance over 3D assemblies without slabs; whereas modelling the 2D assemblies will give a conservative estimate of progressive collapse resistance under column-loss scenarios.

However, there are practical construction cases in which slab contribution to progressive collapse resistance can be ignored such as: (1) when there are openings in slabs; and (2) similar to the local construction practice in many countries around the globe, most of the floor systems are one-way ribbed slabs with ribs spanning either perpendicular or parallel to the exterior RC frames and these ribs are usually topped with very thin RC slab of thickness varying from 50 to 70 mm, and in cases where the ribs are parallel to the exterior RC frames, the top slab cannot be relied upon in progressive collapse resistance in the event of exterior column loss. Therefore, the 2D assemblies have been employed to conduct further parametric studies, as discussed hereafter. The results of these parametric studies are of key importance to the progressive collapse risk of multi-storey buildings in many countries worldwide.

6.2. Effect of column axial load and boundary conditions in 2D assemblies

The validated FE model was extended to study the effect of different boundary-condition parameters on the response of the 2D assemblies under a middle column-removal scenario. The matrix for parametric analysis consisted of 24 specimens with different parameters, *viz.* number of column stories, number of assembly spans, depth of columns C1 and C3, and axial load ratio on the exterior columns (see Table 5). A new relative stiffness parameter (α_s) was first introduced in this study to estimate the development potential of compressive arch and catenary actions in RC SMRFs under abrupt column-removal scenarios. This parameter is defined as:

$$\alpha_s = \frac{\sum k_s}{k_b} = \frac{\sum \left(\frac{E_c I_g}{\ell}\right)_s}{\left(\frac{E_c I_g}{\ell}\right)_b} \tag{4}$$

where $\sum k_s$ = summation of the flexural stiffness of the exterior RC members connected to beam B1 (or B2) at the joint next to the removed column; k_b = stiffness of beam B1 (or B2); E_c = modulus of elasticity of concrete; I_g = moment of inertia of the gross section of concrete about the centroidal axis normal to the plane of the assembly, neglecting reinforcement; ℓ = span length of the RC member.

The analysis matrix was designed to have a wide range of stiffness parameter (α_s), which is ranging from 1.3 to 78.2 (Table 5). The FE mesh for the representative 2D specimens used in the parametric study is shown in Figure 11. The designation of the specimens used in the parametric analysis is such that the acronym 'FDBR'stands for fully developed beam rebars at the exterior joints, the acronym 'CC' denotes continuous columns at the exterior joints (i.e. two-story specimens), the acronym 'BC' symbolizes continuous beams at the exterior joints (i.e. 4-span assembly), the acronyms 'SC1', 'SC2', and 'SC3' represents assemblies with columns C1 and C3 with depths of 300, 400, and 600 mm, respectively, and the numbers '0.0', '0.18', '0.30', and '0.4' represent the axial load ratio applied on top of columns C1 and C3. As illustrated in Table 5, all twenty-four 2D specimens have longitudinal rebars of beams B1 and B2 with full tensile development at the exterior joints. This was achieved numerically by assuming perfect bonding at the rebar-to-concrete interface for nodes lying only beyond the centre line of the outer columns. However, for the rest of the rebar nodes, bond-slip effects were considered as detailed in Sec. 3.

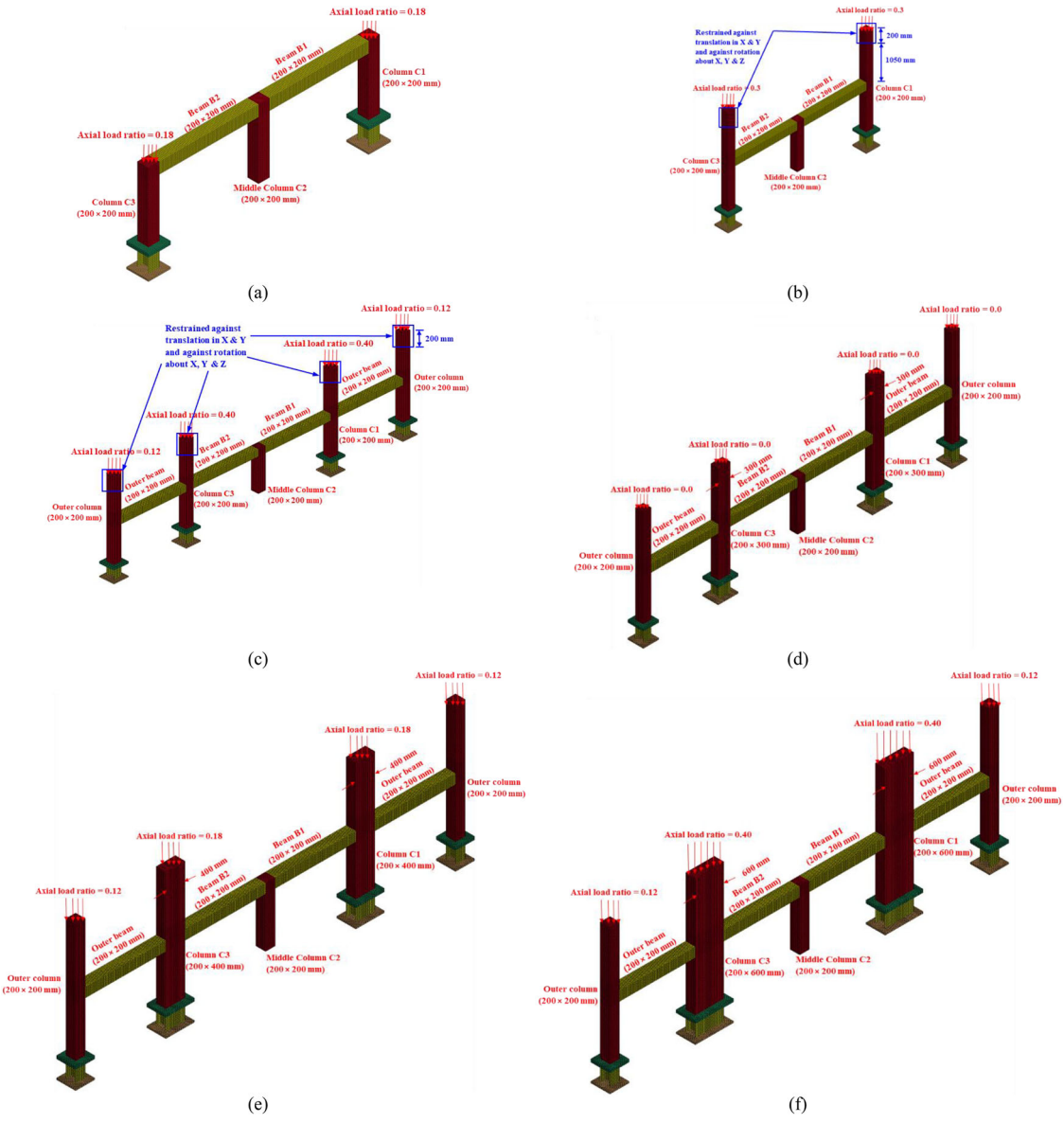

Figure 11. FE mesh for representative 2D specimens: (a) SMRF-2D-FDBR-0.18; (b) SMRF-2D-FDBR-CC-0.30; (c) SMRF-2D-FDBR-CC-BC-0.40; (d) SMRF-2D-FDBR-CC-BC-SC1-0.0; (e) SMRF-2D-FDBR-CC-BC-SC2-0.18; (f) SMRF-2D-FDBR-CC-BC-SC3-0.40.

For the eighteen two-story specimens, columns of the second story were restrained at their top 200-mm length (representing beams traversing the column) against translation in the global X and Y directions, and against rotation about the global X, Y, and Z axes, as seen in Figure 11. Table 5 shows that the effect of beam continuity beyond the exterior joints was only studied for sixteen specimens. Table 5 also depicts that four different sections of columns C1 and C3 were studied with a column depth ranging from 200 to 600 mm. In order to estimate the amount of axial load applied on the columns of the model-scale specimens, a 3D FE model was developed for the eight-story prototype building using ETABS software (2016) with the inclusion of all structural members (beams, columns, and slabs) and different load cases (self-weight, superimposed dead and live loads). The axial load ratio on the columns of the second story of the prototype building at the service load level (the ratio between the axial load on top of the column at the service load level and the axial load capacity of the column section) was estimated. For the corner and exterior columns, this ratio was estimated as 0.12 and 0.18, respectively.

Accordingly, as illustrated in Table 5, four different axial load ratios of 0.0, 0.18, 0.3 and 0.4 were investigated for the exterior columns C1 and C3. However, for the outer columns of four-span assemblies, the axial load ratio was taken as either 0.0 (when the axial load ratio of columns C1 and C3 was 0.0) or 0.12 (when the axial load ratio of columns C1 and C3 ranges from 0.18 to 0.4), as seen in Figure 11. The axial load on the columns of the model-scale specimens was applied on the top nodes of columns as a ramp function, increasing from zero at the onset of the analysis to its peak value at a time of 0.5 s, and then held constant for the rest of the analysis (similar to the gravity load on the slabs shown in Figure 6(a)).

A summary of the analysis results for the twenty-four specimens used in the parametric study is given in Table 6

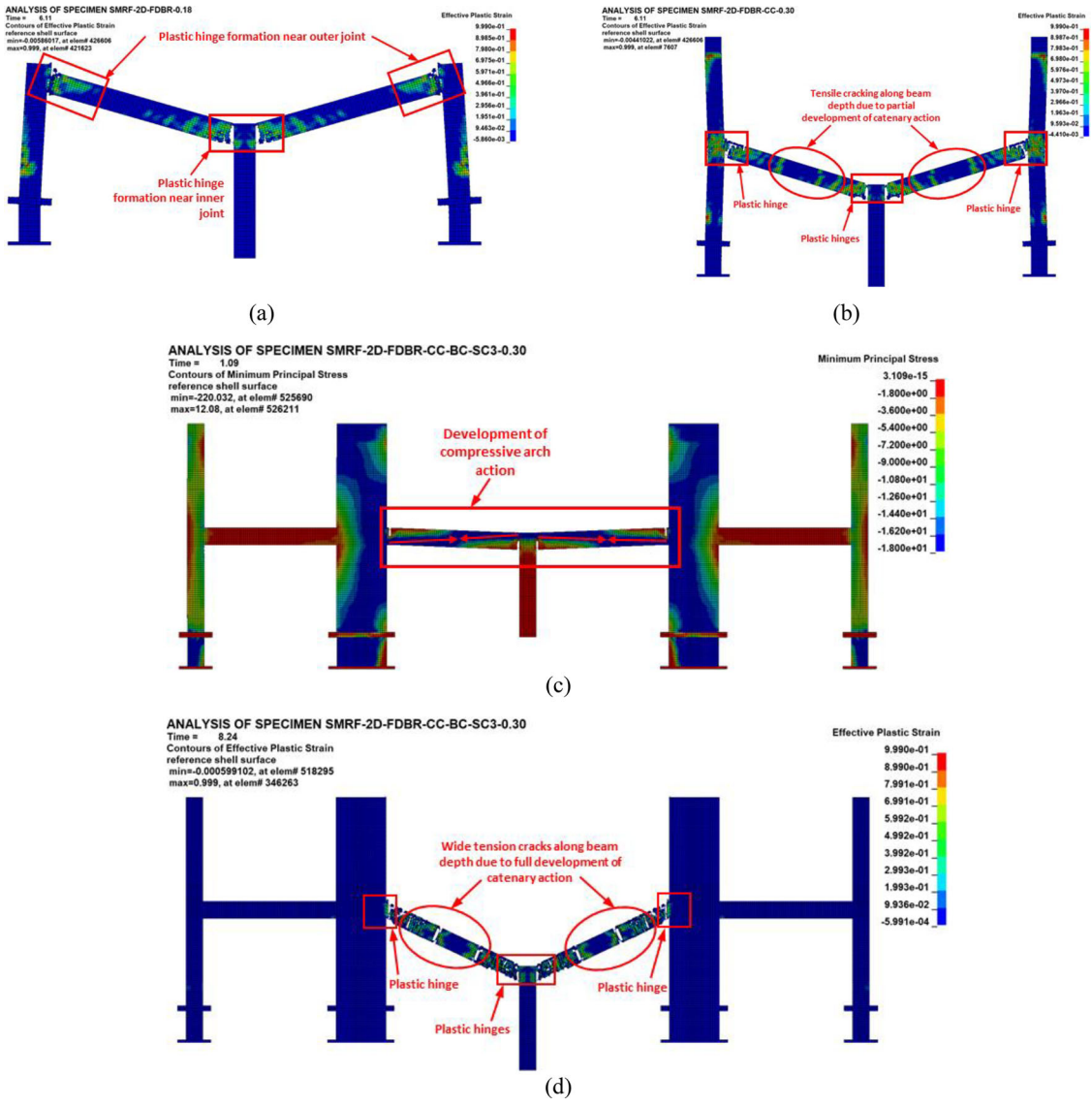

Figure 12. FE mode of failure for representative 2D specimens: (a) Contours of effective plastic strain of specimen SMRF-2D-FDBR-0.18 showing flexural action; (b) Contours of effective plastic strain of specimen SMRF-2D-FDBR-CC-0.30 showing partial development of catenary action; (c) Contours of minimum principal stress of specimen SMRF-2D-FDBR-CC-BC-SC3-0.30 showing development of compressive arch action; (d) Contours of effective plastic strain of specimen SMRF-2D-FDBR-CC-BC-SC3-0.30 showing full development of catenary action.

in terms of all the response parameters at different action stages and ultimate conditions. Figure 12 shows the FE modes of failure for representative samples of 2D specimens. Figures 13(a) to (d) illustrate comparisons between the numerical load and the middle column displacement envelopes for 2D specimens with column axial load ratios of 0.0, 0.18, 0.30, and 0.40, respectively. The evolution of the beam axial force for the twenty-four 2D assemblies used in the parametric study is shown in Figure 14.

It is evident from Table 6 that full development of the longitudinal rebars of beams B1 and B2 inside the exterior columns has increased the peak load capacity of the SMRF-2D specimen by about 17%. From Table 6 and Figure 13, it is also clear that a compressive arch action was not developed for either single-story specimens ($\alpha_s = 1.3$) or two-story, two-span specimens ($\alpha_s = 2.9$). This was also evidenced from Figure 14 for the axial compressive forces in beams B1 and B2. These forces were considerably lower than 10% of the axial beam capacity, which as per the ACI 318-11 code (2011), would not affect the flexural capacity and could thereby be ignored. For the specimens with a column axial load ratio of 0.18 to 0.40, a compressive arch action was developed for all four-span assemblies (α_s ranges from 3.9 to 78.2), as seen in Table 6 and Figure 14. However, for the specimens with columns that have a zero axial load ratio, a compressive arch action was only developed for four-span assemblies with α_s ranging from 11.8 to 78.2.

Figure 15 presents the definitions of different action stages for specimens with and without a compressive arch action. From the figure, it is inferred that for the case with no development of a compressive arch action, catenary action may not exist (e.g. specimen SMRF-2D-FDBR-0.18 (see Figure 12(a))), be partially developed (e.g. specimen SMRF-2D-FDBR-CC-0.30 (see Figure 12(b))) or fully developed (e.g. specimen SMRF-2D-FDBR-CC-BC-0.0). However, in the case where a compressive arch action is developed, catenary action will also be developed (see Figures 12(c) and 12(d)). As seen in Table 6 and Figure 14, catenary action

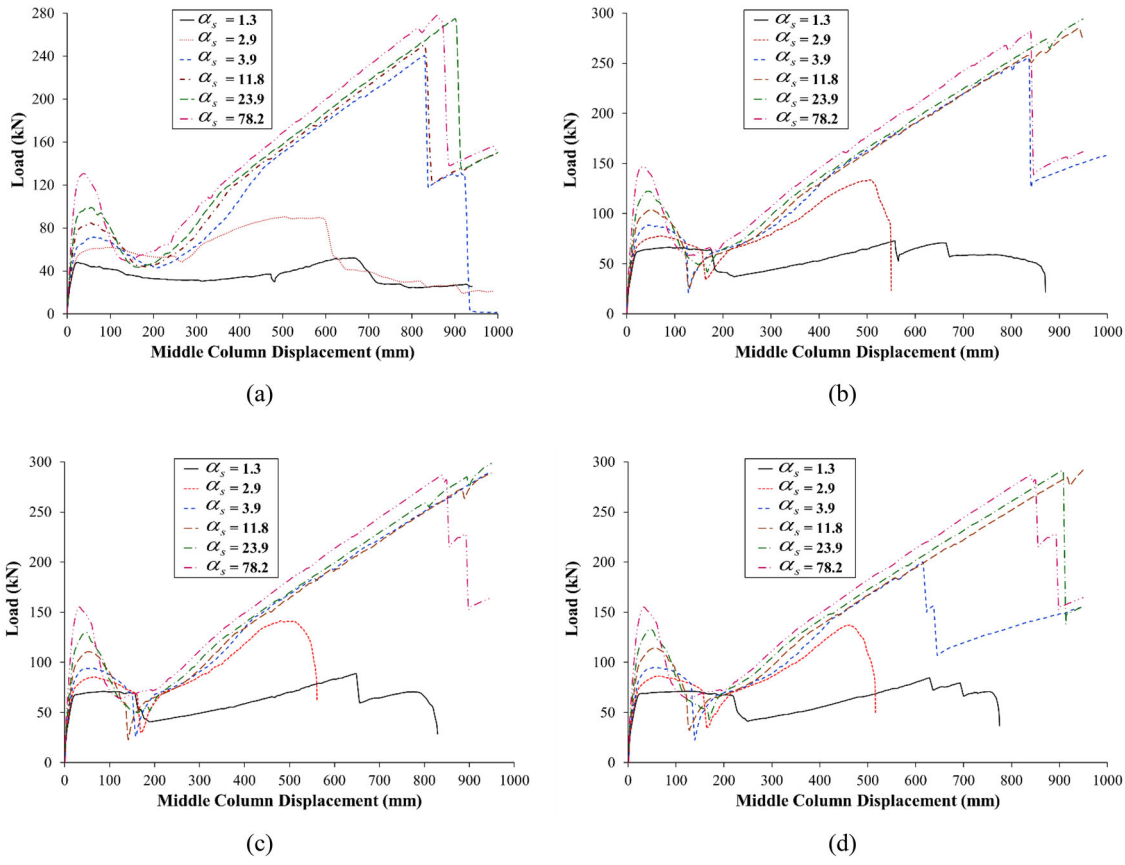

Figure 13. Load-displacement envelopes for 2D specimens with column axial load ratio of: (a) 0.0; (b) 0.18; (c) 0.30; (d) 0.40.

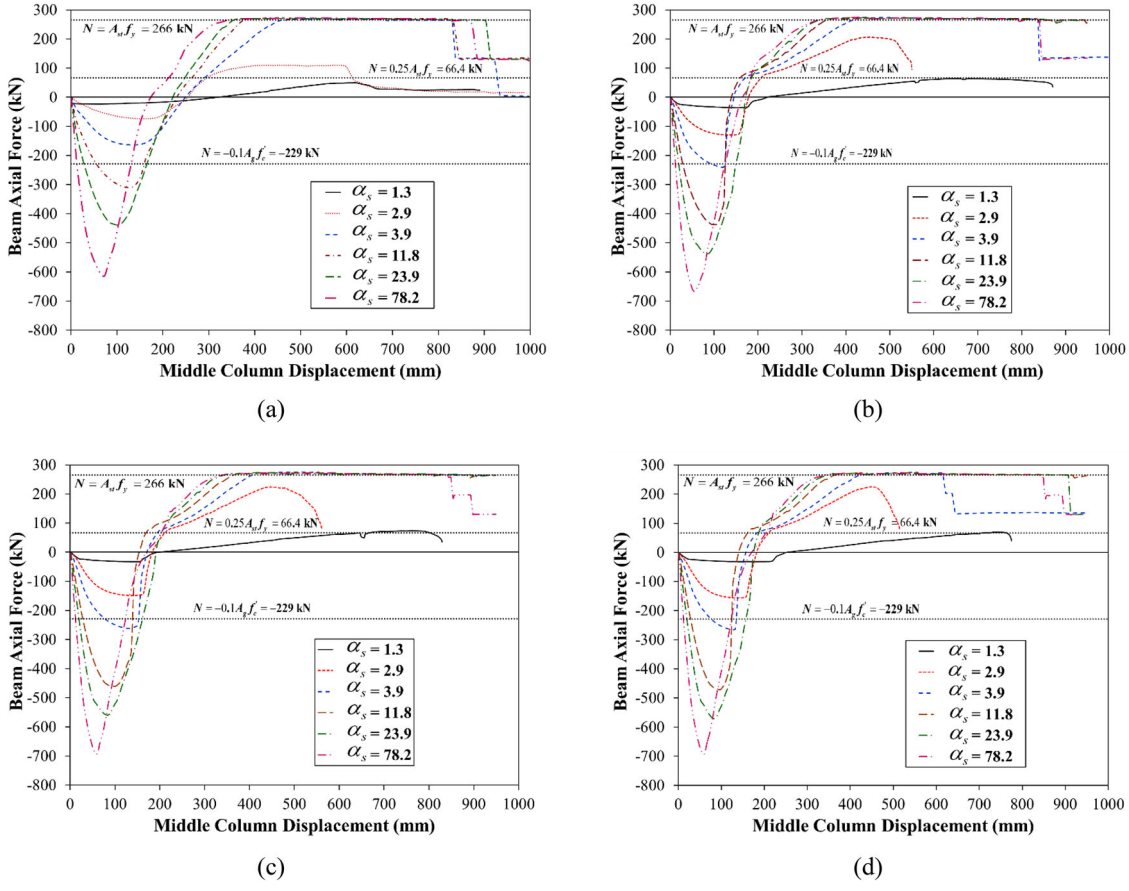

Figure 14. Evolution of beam axial force for 2D specimens with column axial load ratio of: (a) 0.0; (b) 0.18; (c) 0.30; (d) 0.40.

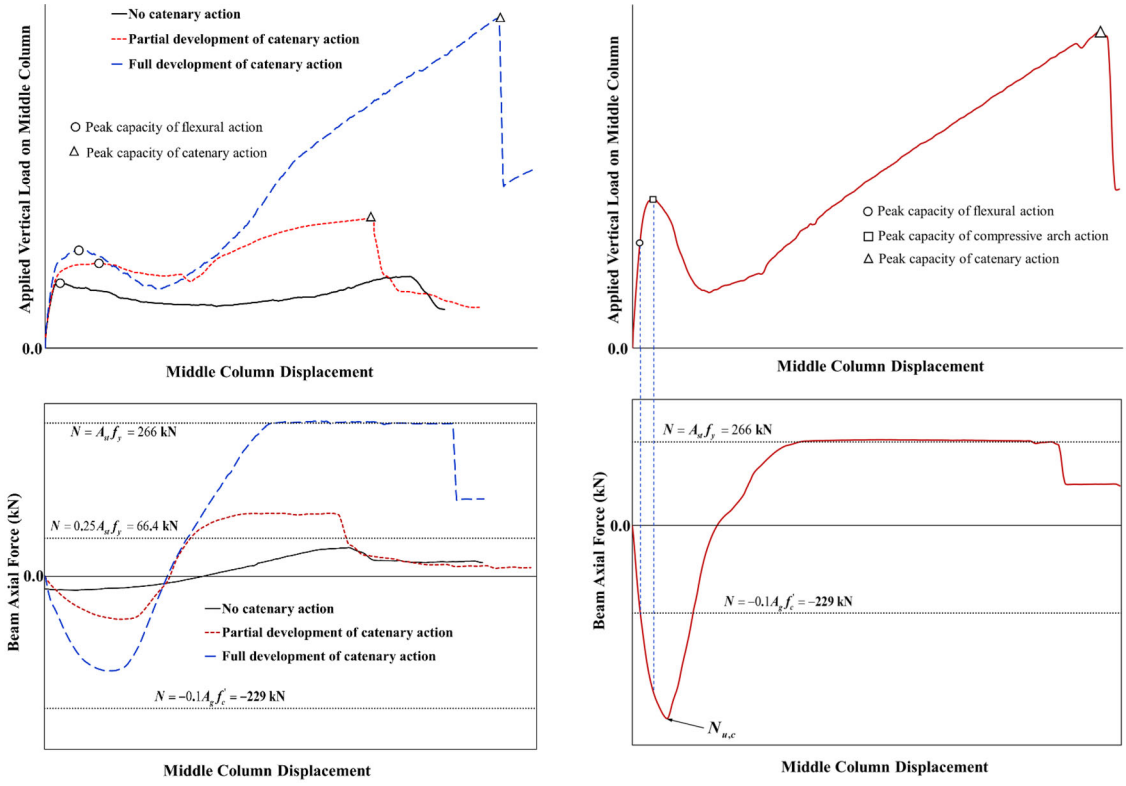

Figure 15. Development of different action stages for: (a) Specimens without compressive arch action; (b) Specimens with compressive arch action.

was not developed for single-story specimens with a column axial load ratio of 0.18 or less. In these specimens, the peak axial tensile force in beams B1 and B2 was well below the force corresponding to the yield strength of a single beam rebar (= 66.4 kN).

As seen in Table 6 and Figure 14, in both single-story specimens with a column axial load ratio exceeding 0.18 and two-story, two-span specimens ($\alpha_s = 2.9$), catenary action was partially developed. In these specimens, the peak axial tension force in beams B1 and B2 was between 66.4 kN (force corresponding to the yield strength of a single beam rebar) and 266 kN (force corresponding to the yield strength of all beam rebars along the full beam span). However, catenary action was fully developed for all four-span assemblies (α_s ranges from 3.9 to 78.2) as the axial load changed from compression to tension and increased to a peak tensile force of 269 to 276 kN (yielding of all beam rebars along the full beam span). For most of the specimens, this tensile force was almost maintained until a large displacement of 800 to 900 mm at which the peak load was attained (Figure 14).

For two-span specimens, increasing the axial load ratio on columns C1 and C3 from 0.0 to 0.18 increased the progressive collapse resistance by 38% and 48%, for single and two-story assemblies, respectively. However, for four-span specimens, increasing the axial load ratio on columns C1 and C3 from 0.0 to 0.18 increased the progressive collapse resistance by 2% to 14%, as seen in Table 6. For most of the 2D specimens, it was found that increasing the axial load ratio on columns C1 and C3 from 0.18 to 0.4 has a marginal effect on the progressive collapse resistance. Accordingly and in line with the ACI 318-11 code, the 2D assemblies can be mainly categorized into two groups, *viz.* specimens with a column axial load ratio ≤ 0.10 (axial load ratio = 0.0 in this case) and those with a column axial load ratio > 0.10 (three specimens for this case). The results of the second group can thereby be averaged to give a single value.

For assessing the potential for compressive arch action development in 2D SMRF assemblies, the relationship between the stiffness parameter (α_s) and peak compression axial force ratio of beams B1 and B2 ($\frac{N_{u,c}}{A_g f'_c}$ where $N_{u,c}$ is the peak compression axial force of beams B1 and B2; A_g is the gross area of the concrete section of beams B1 and B2) was generated, as seen in Figure 16(a), for the two groups of specimens identified above. For the case of column axial load ratio ≤ 0.10, compressive arch action was developed for assemblies with $\alpha_s > 7.4$. Nevertheless, when column axial load ratio is greater than 0.10, compressive arch action was developed for assemblies with $\alpha_s > 3.6$. Figure 16(b) illustrates the correlation between the stiffness parameter α_s and ratio of the peak load of the compressive arch action stage to the peak load of the flexural action stage. For assemblies with a column axial load ratio ≤ 0.10, due to the compressive arch action, the peak load increased by 41% for $\alpha_s = 78.2$. However, for specimens with a column axial load ratio > 0.10, the compressive arch action increased the peak load by 54% for $\alpha_s = 78.2$.

Figure 17(a) presents the relationship between the stiffness parameter (α_s) and peak tension axial force ratio of

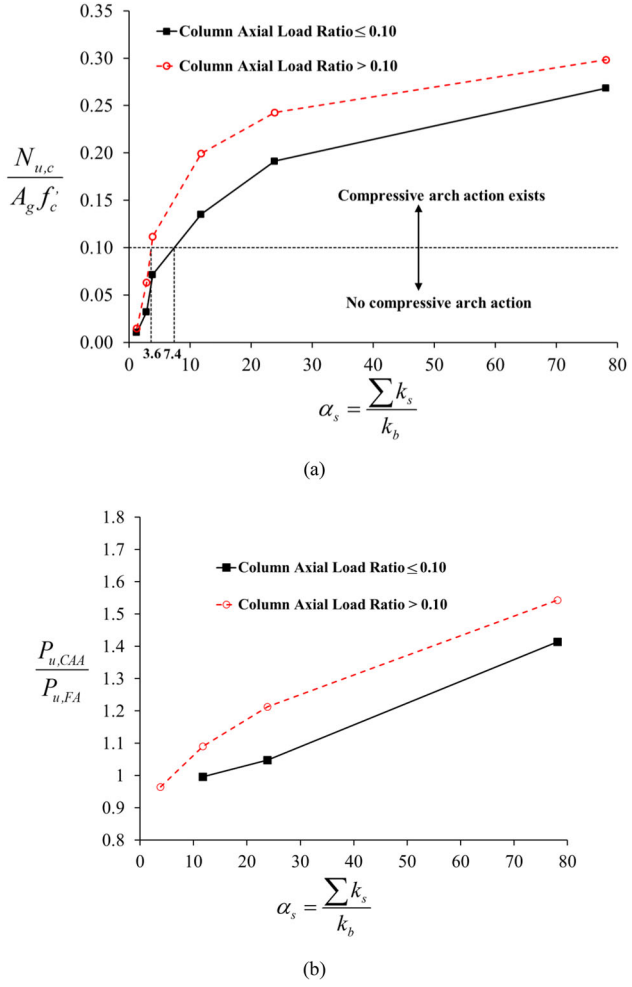

Figure 16. Effect of beam relative stiffness (α_s) on: (a) Development of compressive arch action; (b) Increase of peak load due to compressive arch action.

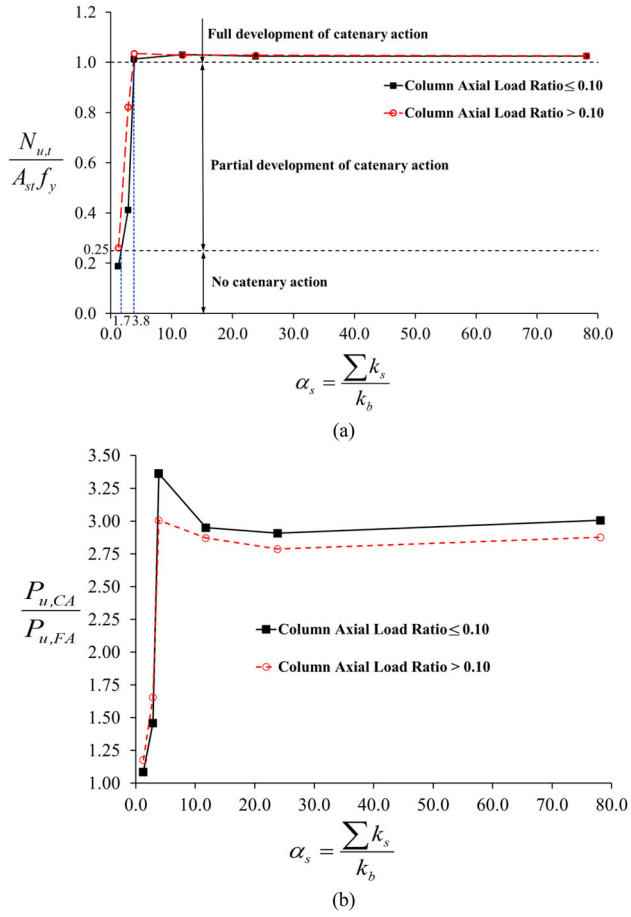

Figure 17. Effect of beam relative stiffness (α_s) on: (a) Development of catenary action; (b) Increase of peak load due to catenary action.

beams B1 and B2 ($\frac{N_{u,t}}{A_{st}f_y}$ where $N_{u,t}$ is the peak axial tensile force of beams B1 and B2; A_{st} is the total area of the top and bottom longitudinal steel rebars of beam B1 (or B2); and f_y is the yield strength of the longitudinal beam rebars). For the case with a column axial load ratio $\leq$ 0.10, catenary action was not developed for assemblies with $\alpha_s < 1.7$. However, catenary action was partially developed for $1.7 \leq \alpha_s < 3.8$. For $\alpha_s \geq 3.8$, catenary action was fully developed, as seen in Figure 17(a). For the case with a column axial load ratio $>$ 0.10, catenary action was partially developed for assemblies with $1.3 \leq \alpha_s < 3.8$ and it was fully developed for those with $\alpha_s \geq 3.8$. Figure 17(b) illustrates the relationship between the stiffness parameter α_s and ratio of peak load of the catenary action stage to the peak load of the flexural action stage. In all cases, it is evident that full development of catenary action increased the peak load by 188% to 236%.

In conclusion, it is noted that increasing the axial compression ratio of the columns is able to affect the mobilization of compressive arch action of beams. As stated by many codes and researchers (ASCE/SEI 41-06, 2006; Elwood & Eberhard, 2009; FEMA 356, 2000; Paulay & Priestley, 1992; Tran & Li, 2012), the effective flexural stiffness of RC columns increases with the increase in their axial compression load ratio. Therefore, increasing the axial compression ratio of the exterior RC columns will increase the summation of the effective flexural stiffness of the exterior RC members connected to exterior beams at the joint next to the removed column. This will add more restraint to that joint, thereby mobilizing the compressive arch action in exterior RC beams connected to the lost column.

7. Conclusions

The following main conclusions can be derived from this study:

1. The FE model used in this study was found appropriate for assessing the progressive collapse resistance of RC SMRFs under a column-removal scenario. This validates the FE modeling approach, which may be reliably employed for progressive collapse assessment of ordinary and intermediate RC moment resisting frame structures.
2. A perfect bonding assumption for the rebar-to-concrete interface overestimates the progressive collapse resistance of RC assemblies subjected to column removal. For proper prediction of the progressive collapse resistance, bond-slip effects must be modeled at least between the concrete and longitudinal rebars of beams and slabs connected to the removed column.
3. Modeling RC slabs in the 3D assemblies significantly increased the progressive collapse resistance over 3D

assemblies without slabs. Modeling of the 2D assemblies will give a conservative estimate of the progressive collapse resistance under column-loss scenarios.

4. A new relative stiffness parameter (α_s) was first introduced in this study. This parameter is defined as the ratio of the total flexural stiffness of exterior RC members connected to the exterior frame beam attached to the removed column to the flexural stiffness of that beam. This parameter was used to assess the development potential of compressive arch and catenary actions in RC SMRFs under abrupt column-removal scenarios. For the case of the axial load ratio of the column adjacent to the removed column ≤ 0.10, compressive arch action was developed for assemblies with $\alpha_s > 7.4$. However, for the case with a column axial load ratio > 0.10, compressive arch action was developed for assemblies with $\alpha_s > 3.6$. It was also noticed that in the case of no development of a compressive arch action, catenary action may not exist (for $\alpha_s < 1.7$ (or 1.3) in case with a column axial load ratio ≤ 0.10 (or > 0.10), respectively), be partially developed (for α_s ranging from 1.7 (or 1.3) to 3.8 in case of column axial load ratio ≤ 0.10 (or > 0.10), respectively) or fully developed (for $\alpha_s \geq 3.8$). However, in the case where a compressive arch action is developed, catenary action will be also fully developed.

Acknowledgement

The authors are grateful to the Deanship of Scientific Research, King Saud University, for funding through Vice Deanship of Scientific Research Chairs.

Disclosure statement

The authors declare that they have no conflict of interest.

References

Abbas, H., Al-Salloum, Y. A., & Almusallam, T. H. (2017). Precast reinforced concrete construction elements with pre-stressing connectors. U.S. Patent. No. 9765521 B1, U.S. Patent and Trademark Office.

ACI 318-11. (2011). *Building code requirements for structural concrete and commentary*. Detroit, MI: American Concrete Institute.

Almusallam, T., Al-Salloum, Y., Elsanadedy, H., Iqbal, R., Abbas, H., & Siddiqui, N. (2016). Risk assessment of precast reinforced concrete buildings against blast loads: a case study. In *Insights and innovations in structural engineering, mechanics and computation*. London, UK: Taylor & Francis Group.

Almusallam, T., Al-Salloum, Y., Ngo, T., Mendis, P., & Abbas, H. (2017). Experimental investigation of progressive collapse potential of ordinary and special moment-resisting reinforced concrete frames. *Materials and Structures*, *50*(2), 137. doi:10.1617/s11527-017-1014-x

Almusallam, T. H., Elsanadedy, H. M., Abbas, H., Alsayed, S. H., & Al-Salloum, Y. A. (2010). Progressive collapse analysis of a RC building subjected to blast loads. *Structural Engineering and Mechanics*, *36*(3), 301–319. doi:10.12989/sem.2010.36.3.301

Almusallam, T. H., Elsanadedy, H. M., Abbas, H., Ngo, T., & Mendis, P. (2010). Numerical analysis for progressive collapse potential of a typical framed concrete building. *International Journal of Civil & Environmental Engineering*, *10*(2), 36–42.

Al-Salloum, Y. A., Abbas, H., Almusallam, T. H., Ngo, T., & Mendis, P. (2017). Progressive collapse analysis of a typical RC high-rise tower. *Journal of King Saud University - Engineering Sciences*, *29*(4), 313–320. doi:10.1016/j.jksues.2017.06.005

Al-Salloum, Y. A., Almusallam, T. H., Khawaji, M. Y., Ngo, T., Elsanadedy, H. M., & Abbas, H. (2015). Progressive collapse analysis of RC buildings against internal blast. *Advances in Structural Engineering*, *18*(12), 2181–2192. doi:10.1260/1369-4332.18.12.2181

Al-Salloum, Y. A., Alrubaidi, M. A., Elsanadedy, H. M., Almusallam, T. H., & Iqbal, R. A. (2018). Strengthening of precast RC beam-column connections for progressive collapse mitigation using bolted steel plates. *Engineering Structures*, *161*, 146–160. doi:10.1016/j.engstruct.2018.02.009

ASCE/SEI 41-06. (2006). *Seismic rehabilitation of existing buildings*. Reston, VA: American Society of Civil Engineers,.

ASCE/SEI 7-16. (2016). *Minimum design loads and associated criteria for buildings and other structures*. Reston, VA: American Society of Civil Engineers,.

Bao, Y., Lew, H. S., & Kunnath, S. K. (2014). Modeling of reinforced concrete assemblies under column-removal scenario. *Journal of Structural Engineering*, *140*(1), 04013026. doi:10.1061/(ASCE)ST.1943-541X.0000773

Belytschko, T., Lin, J. I., & Chen-Shyh, T. (1984). Explicit algorithms for the nonlinear dynamics of shells. *Computer Methods in Applied Mechanics and Engineering*, *42*(2), 225–251. doi:10.1016/0045-7825(84)90026-4

CEN. (2002). *Eurocode 1, Actions on structures*. Brussels, Belgium: European Committee for Standardization.

Choi, H., & Kim, J. (2011). Progressive collapse-resisting capacity of RC beam–column sub-assemblage. *Magazine of Concrete Research*, *63*(4), 297–310. doi:10.1680/macr.9.00170

de Witte, F. C. (2005). *User's manual – release 9*. Delft, the Netherlands: TNO DIANA BV.

DOD. (2005). Unified facilities criteria, design of building to resist progressive collapse, Department of Defense, USA.

Ellingwood, B. R. (2006). Mitigating risk from abnormal loads and progressive collapse. *Journal of Performance of Constructed Facilities*, *20*(4), 315–323. doi:10.1061/(ASCE)0887-3828(2006)20:4(315)

Elsanadedy, H. M., Almusallam, T. H., Alharbi, Y. R., Al-Salloum, Y. A., & Abbas, H. (2014). Progressive collapse potential of a typical steel building due to blast attacks. *Journal of Constructional Steel Research*, *101*, 143–157. doi:10.1016/j.jcsr.2014.05.005

Elsanadedy, H. M., Almusallam, T. H., Al-Salloum, Y. A., & Abbas, H. (2017). Investigation of precast RC beam-column assemblies under column-loss scenario. *Construction and Building Materials*, *142*, 552–571. doi:10.1016/j.conbuildmat.2017.03.120

Elwood, K. J., & Eberhard, M. O. (2009). Effective stiffness of reinforced concrete columns. *ACI Structural Journal*, *106*(4), 476–484.

ETABS. (2016). Computers and Structures, Inc. ETABS 2016 16.2.0 – extended 3D analysis of building systems. Berkeley, CA, USA.

FEMA 356. (2000). *Prestandard and commentary for the seismic rehabilitation of buildings*, Washington DC: Federal Emergency Management Agency.

FEMA 426. (2003). *Reference manual to mitigate potential terrorist attacks against buildings*. Washington DC: US Federal Emergency Management Agency.

GSA. (2013). Alternate path analysis & design guidelines for progressive collapse resistance. General Service Administration, The U.S. General Services Administration.

IBC. (2000). *International building code*. International Code Council, Inc., International Conference of Building Officials, Whittier, CA.

ISC. (2001). ISC Security criteria for new federal office buildings and major modernization projects. The Interagency Security Committee.

Kang, S. B., & Tan, K. H. (2016). Analytical model for compressive arch action in horizontally restrained beam-column subassemblages. *ACI Structural Journal*, *113*(4), 813–826. doi:10.14359/51688629

Kim, J., & An, D. (2009). Evaluation of progressive collapse potential of steel moment frames considering catenary action. *The Structural*

Design of Tall and Special Buildings, *18*(4), 455–465. doi:10.1002/tal.448

Kim, J., & Kim, T. (2009). Assessment of progressive collapse-resisting capacity of steel moment frames. *Journal of Constructional Steel Research*, *65*(1), 169–179. doi:10.1016/j.jcsr.2008.03.020

Kim, J., & Yu, J. (2012). Analysis of reinforced concrete frames subjected to column loss. *Magazine of Concrete Research*, *64*(1), 21–33. doi:10.1680/macr.2012.64.1.21

Lew, H. S., Bao, Y., Pujol, S., & Sozen, M. A. (2014). Experimental Study of Reinforced Concrete Assemblies under Column Removal Scenario. *ACI Structural Journal*, *111*(4), 881–892. doi:10.14359/51686739

Lim, N. S., Tan, K. H., & Lee, C. K. (2017). Experimental studies of 3D RC substructures under exterior and corner column removal scenarios. *Engineering Structures*, *150*, 409–427.

Liu, Y., Xu, L., & Grierson, D. E. (2008). Compound-element modeling accounting for semi-rigid connections and member plasticity. *Engineering Structures*, *30*(5), 1292–1307. doi:10.1016/j.engstruct.2007.07.026

LS-DYNA (2007). *Livermore Software Technology Corporation (LSTC). LS-DYNA user's keyword manual (nonlinear dynamic analysis of structures in three dimensions)* Vol. 1. Version 971, Livermore, CA: LSTC.

Lu, X., Lin, K., Li, Y., Guan, H., Ren, P., & Zhou, Y. (2017). Experimental investigation of RC beam-slab substructures against progressive collapse subject to an edge-column-removal scenario. *Engineering Structures*, *149*, 91–103. doi:10.1016/j.engstruct.2016.07.039

Marjanishvili, S., & Agnew, E. (2006). Comparison of various procedures for progressive collapse analysis. *Journal of Performance of Constructed Facilities*, *20*(4), 365–374. doi:10.1061/(ASCE)0887-3828(2006)20:4(365)

Milner, D., Gran, J., Lawver, D., Vaughan, D., Vanadit-Ellis, W., & Levine, H. (2007). FLEX analysis and scaled testing for prediction of progressive collapse. In first international workshop on performance, protection & strengthening of structures under extreme loading (PROTECT 2007), Whistler, Canada.

Murray, Y. D., Abu-Odeh, A., & Bligh, R. (2007). Evaluation of concrete material model 159. Report No. FHWA-HRT-05-063, US Department of Transportation, Federal Highway Administration National Transportation Systems Center, USA.

Ngo, T., Mendis, P., Gupta, A., & Ramsay, J. (2007). Blast loading and blast effects on structures–an overview. *Electronic Journal of Structural Engineering*, *7*(S1), 76–91.

NRCC. (1995). *National building code of Canada*. Ottawa, Canada: National Research Council of Canada,.

NZS 4203. (1992). *Code of practice for general structural design and design loadings for buildings*. New Zealand: New Zealand Standard.

Paulay, T., & Priestley, M.J.N. (1992). *Seismic design of reinforced concrete masonry buildings*. New York, NY: John Willey & Sons.

Pearson, C., & Delatte, N. (2005). Ronan point apartment tower collapse and its effect on building codes. *Journal of Performance of Constructed Facilities*, *19*(2), 172–177. doi:10.1061/(ASCE)0887-3828(2005)19:2(172)

Sasani, M., Bazan, M., & Sagiroglu, S. (2007). Experimental and analytical progressive collapse evaluation of actual reinforced concrete structure. *ACI Structural Journal*, *104*(6), 731–739.

Sasani, M., & Kropelnicki, J. (2008). Progressive collapse analysis of an RC structure. *The Structural Design of Tall and Special Buildings*, *17*(4), 757–771. doi:10.1002/tal.375

SBC 301. (2007). Loads & forces requirements. Saudi Building Code National Committee, Saudi Arabia.

SBC 304. (2007). Concrete structures requirements, Saudi Building Code National Committee, Saudi Arabia.

Tran, C. T. N., & Li, B. (2012). Initial stiffness of reinforced concrete columns with moderate aspect ratios. *Advances in Structural Engineering*, *15*(2), 265–276. doi:10.1260/1369-4332.15.2.265

Tsai, M. H., & Lin, B. H. (2008). Investigation of progressive collapse resistance and inelastic response for an earthquake-resistant RC building subjected to column failure. *Engineering Structures*, *30*(12), 3619–3628. doi:10.1016/j.engstruct.2008.05.031

Xiao, Y., & Rui M. (1997). Seismic retrofit of RC circular columns using prefabricated composite jacketing. *Journal of Structural Engineering*, *123*(10), 1357–1364. doi:10.1061/(ASCE)0733-9445(1997)123:10(1357)

Yi, W. J., He, Q. F., Xiao, Y., & Kunnath, S. K. (2008). Experimental study on progressive collapse-resistant behavior of reinforced concrete frame structures. *ACI Structural Journal*, *105*(4), 433–439.

Yu, J., Luo, L., & Li, Y. (2018). Numerical study of progressive collapse resistance of RC beam-slab substructures under perimeter column removal scenarios. *Engineering Structures*, *159*, 14–27. doi:10.1016/j.engstruct.2017.12.038

Yu, J., Rinder, T., Stolz, A., Tan, K. H., & Riedel, W. (2014). Dynamic progressive collapse of an RC assemblage induced by contact detonation. *Journal of Structural Engineering*, *140*(6), 04014014.

Yu, J., & Tan, K. H. (2013). Experimental and numerical investigation on progressive collapse resistance of reinforced concrete beam column sub-assemblages. *Engineering Structures*, *55*, 90–106. doi:10.1016/j.engstruct.2011.08.040

Yu, J., & Tan, K. H. (2014). Analytical model for the capacity of compressive arch action of reinforced concrete sub-assemblages. *Magazine of Concrete Research*, *66*(3), 109–126. doi:10.1680/macr.13.00217

Yu, J., & Tan, K. H. (2017). Structural behavior of reinforced concrete frames subjected to progressive collapse. *ACI Structural Journal*, *114*(1), 63–74. doi:10.14359/51689424

Zheng et al. (2013). Chinese Patent No. CN 203230191 U, National Intellectual Property Administration, People's Republic of China.